Flow Turbulence Combust (2013) 90:29–68
DOI 10.1007/s10494-012-9421-0

Immersed Boundaries in Large Eddy Simulation of Compressible Flows

Cindy Merlin · Pascale Domingo · Luc Vervisch

Received: 12 October 2011 / Accepted: 4 October 2012 / Published online: 2 November 2012

Abstract Methods to immerse walls in a structured mesh are examined in the context of fully compressible solutions of the Navier–Stokes equations. The ghost cell approach is tested along with compressible conservative immersed boundaries in canonical flow configurations; the reflexion of pressure waves on walls arbitrarily inclined on a cartesian mesh is studied, and mass conservation issues examined in both a channel flow inclined at various angles and flow past a cylinder. Then, results from Large Eddy Simulation of a flow past a rectangular cylinder and a transonic cavity flow are compared against experiments, using either a multi-block mesh conforming to the wall or immersed boundaries. Different strategies to account for unresolved transport by velocity fluctuations in LES are also compared. It is found that immersed boundaries allow for reproducing most of the coupling between flow instabilities and pressure-signal properties observed in the transonic cavity flow. To conclude, the complex geometry of a trapped vortex combustor, including a cavity, is simulated and results compared against experiments.

Keywords Large Eddy Simulation · Compressible flow · Immersed boundaries

1 Introduction

Handling complex geometries on structured and cartesian grids has been the subject of many studies; specifically motivated by flow simulations over fixed or moving objects of highly complex shape, leading to challenging transformations if curvilinear coordinates are used or to discretization errors with body-fitted grids, because of eventual non-perfect cell-alignment with the wall. First discussed in the context of blood flow [53], many strategies have been developed to mimick the presence

C. Merlin · P. Domingo (✉) · L. Vervisch
CORIA - CNRS & INSA de Rouen, Campus du Madrillet, Saint-Etienne-du-Rouvray, 76800, France
e-mail: domingo@coria.fr

of walls inside a fixed mesh, by adding a continuous forcing term in the balance equations [3, 21, 31, 48, 67] or through a specific treatment of their discretized form, by modifying the computational stencil near the immersed object [1, 16, 17, 26, 32, 34, 41, 45, 47, 48, 67, 70].

Immersed boundaries with compressible flows have been addressed at some places in the literature [9, 16, 17, 52], but most of the published works on the subject focus on incompressible or variable density flows. In the present paper, an attempt is made to combine immersed boundaries, grounded on the ghost cell technique, with the solution of the Navier–Stokes equations in their fully compressible form. The difficulty then lies in the treatment, over the immersed wall, of the strong coupling between energy conservation and the acoustic field, with feedback into momentum budget.

The elementary bricks of the retained method are discussed before considering canonical test cases; the ghost cell formalism is used with some adjustments to ensure a wall-response to acoustic perturbation close to the one observed with boundary conditions imposed on a mesh conforming to wall. This is done simulating propagation of a spherical pressure wave in a three-dimensional enclosure. In contrary to constant-density flow-solvers, mass conservation is not explicitly imposed to the fully compressible velocity solution and the accuracy of the mass budget is also examined for both, a flow past a cylinder and a channel flow inclined at various angles in a fixed horizontal cartesian mesh.

The computation of large-scale flow motion with Large Eddy Simulation (LES) using immersed boundaries is then addressed, comparing five sub-grid scale (SGS) modeling of the transport by unresolved velocity fluctuations, with some discussion on filtering operations in the presence of immersed walls. Results of a flow passing a rectangular cylinder and the more stringent transonic cavity-flow test case, are compared against experiments. In the latter, measured information on pressure spectra is found to be reproduced with the proposed immersed boundary strategy. Finally, the flow inside a trapped vortex combustor is simulated to compare flow statistics against measurements in a complex geometry featuring flame holders followed by a cavity.

The paper is organized as follow, the sub-grid scale modeling and the numerics used are summarized in a first section; the details of the immersed boundary approach are given in a subsequent section. Reference test cases (pressure-wave reflexion, flow past a confined cylinder, channel whose inclination on the mesh varies) are analyzed in the next section, together with LES of the flow past a rectangular cylinder. LES of a transonic cavity flow experimentally studied [15] is then examined, comparing results from walls arbitrarily imposed on a given mesh through immersed boundaries, and, a multi-block simulation using a wall-conforming mesh. The trapped vortex combustor simulation is reported in a final section.

2 Sub-Grid Scale Modeling and Numerics

The structured-grid and explicit finite volume fully compressible flow solver SiTCom [10, 38, 39, 61] has been used. The Navier–Stokes equations (conservation of mass, momentum and energy) are solved in their fully compressible form without any preconditioning. The convective terms are computed resorting to a fourth-order

centered skew-symmetric-like scheme [12], while the diffusive terms are discretized with a fourth-order centered scheme. Time is advanced with a third-order Runge–Kutta method [22] and the boundary conditions are prescribed with 3D-NSCBC [38]. In the turbulent flow cases studied, synthetic velocity fluctuations are imposed at the inlet of the computational domain [30].

Large Eddy Simulation, where large-scale flow motion is simulated while the effect of unresolved smaller scales is modeled, may be conducted explicitly, after formulating a physical model for the unresolved transport by velocity fluctuations, or, in a more implicit manner, which relies on a dissipative numerical scheme to mimic the smallest-scales viscous contribution [55].

For the transonic flow past a cavity test case, a first set of simulations have been performed with an eddy viscosity hypothesis [60], combined with three procedures to estimate, ν_T, the SGS viscosity: Vreman et al. closure [69], Lagrangian Dynamic Model [44] and Localized Dynamic Smagorinsky Model [18]. In all cases, the deviatoric part of $\tau_{ij} = \overline{\rho u_i u_j} - \overline{\rho}\widetilde{u}_i\widetilde{u}_j$, the SGS stresses, reads:

$$\tau_{ij}^d = \tau_{ij} - \frac{1}{3}\tau_{kk}\delta_{ij} = -2\overline{\rho}\nu_T\widetilde{A}_{ij}, \tag{1}$$

where ν_T is obtained from its modeled expression and $A_{ij} = (\partial u_i/\partial x_j + \partial u_j/\partial x_i)/2 - (\partial u_k/\partial x_k)\delta_{ij}/3$. An additional modeling is introduced for the isotropic part τ_{kk} [71]:

$$\tau_{kk} = 2C_I\overline{\rho}\Delta^2|\widetilde{S}|^2, \tag{2}$$

$|\overline{S}| = \sqrt{2\widetilde{S}_{ij}\widetilde{S}_{ij}}$ is the magnitude of $S_{ij} = A_{ij} + (\partial u_k/\partial x_k)\delta_{ij}/3$, the strain-rate tensor, and Δ is the LES filter size. Both C_I and the turbulent Prandlt number [49] are also computed with their specific dynamic procedure [39], according to the modeling considered. LES of the flow past a rectangular cylinder is performed with the WALE [51] closure.

A second set of calculations has been carried out with implicit Large Eddy Simulation [55]; grounded on the observation that SGS modeling mostly plays a dissipative role in the simulations, as numerical artificial dissipation would. An artificial dissipation scheme was selected [27], which introduces second and/or fourth order dissipative terms whose global contribution is somehow similar to subgrid scale modeling [55]. To compute the transonic cavity featuring quite strong pressure and density discontinuities, both calculations (implicit or explicit LES) need moderate second-order dissipation. However in the implicit LES, the fourth-order dissipation term is increased, to damp high frequency modes appearing in the centered scheme [62]. As these modes develop at small scales, they are naturally dissipated by the SGS model in explicit LES, canceling the need of additional fourth order dissipative terms.

The skew symmetric scheme used being centered [12], it is non-dissipative. As discussed above, this scheme is completed by an addition of second- and fourth-order artificial dissipation terms [27, 62, 63], involving an additional numerical convective flux that is controlled by four parameters α_1, α_2, β_1 and β_2. The coefficients $\alpha_1 = 0.5$ and $\alpha_2 = 0.5$ are for the second-order terms, β_1 and β_2 for the fourth-order contribution [63]. α_1 controls upwinding fluxes, while α_2 pilots the switch to upwind diffusion for a threshold value of a sensor based on pressure fluctuations [27]. β_1 characterizes the strength of the fourth-order damping and $\beta_2 = 1$ is set to switch off the fourth-order damping in case of strong discontinuities. For DNS, β_1 is set to

0.016, LES with explicit SGS modeling is performed with $\beta_1 = 0.032$ and β_1 is fixed at 0.25 for implicit LES. It has been verified that slightly modifying these values does not profoundly impact on results.

3 Immersed Boundary Method

In the simulations reported below, a solid Γ-surface is immersed into a Cartesian grid and a proper wall boundary condition must be imposed to the surrounding flow, this is done with a ghost cell technique [1, 13, 17, 26, 65]. The key features of this approach are summarized in this section.

Three types of cells are identified: fluid cells (Ω_f), cells inside the solid domain (Ω_s) and ghost cells at the boundary, on the solid side (Fig. 1). The value of a signed distance function $d(x, y, z, t)$ from the solid Γ-surface is computed for every cell; $d > 0$ indicates fluid cells, $d < 0$ are the solid cells and the ghost cells are those bordering

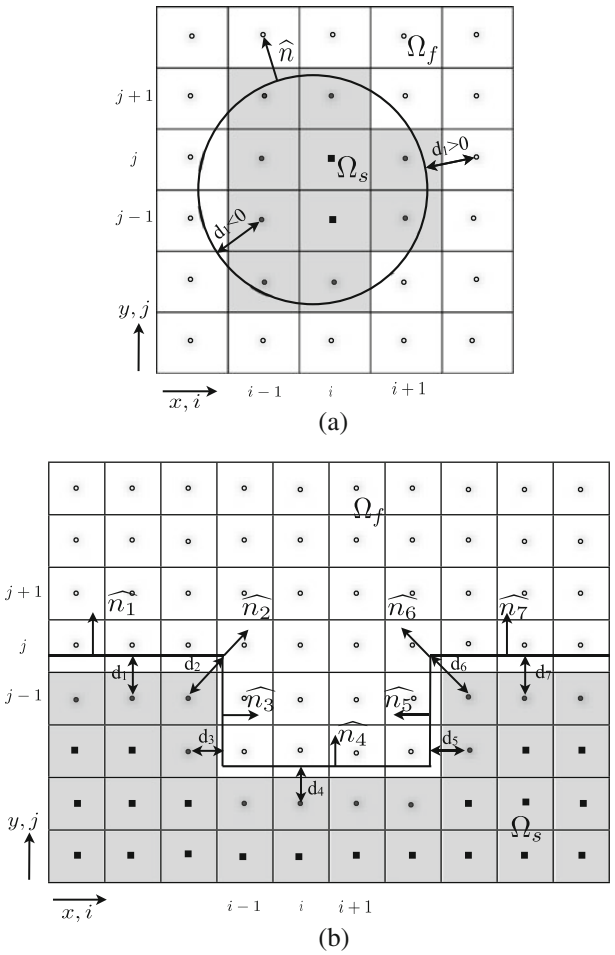

Fig. 1 Cells identification; *Open circle*: fluid cell, *Filled square*: Solid cell, *Filled circle*: Ghost cell. **a** Sharp-angle free geometries require one signed distance function. **b** Corners require specific distance functions definition (d_2 and d_6)

the fluid (where the d sign has changed, see Fig. 1). The immersed boundary method computes the flow at the ghost cells so that the fluid cells account for the precise position of the wall boundary.

Depending on the complexity of the geometry, one or more distance functions may be needed to capture the various surface patches. These distance functions may be prescribed analytically, in the case of simple interfaces, or constructed numerically for complex surfaces [8, 47]. In the case of various distance functions, the retained d level-set corresponds to the minimum distance between the considered cell point and the interface. Any geometry can then be described into a number of piecewise elements. The use of the zero level-set value of the distance function is nevertheless excluded for sharp corners or very thin object. To handle such irregular boundaries, the level-set formulation may be kept unchanged, to modify only the ghost cell approach extending the solution across the boundary for each discretized direction [2]. However, if difficulties only arise because or corners, computing d from the effective distance between the corner position and the grid cell, as depicted in Fig. 1, may be sufficient.

Φ_G, the value of a given flow variable at a ghost cell located at x_k, is computed by imposing a specific condition Φ_Γ over the Γ-surface, to relate Φ_G to Φ_{IP}, the flow variable at IP, the 'image point' of the ghost cell (Fig. 2a). IP lies on the normal to the Γ-surface, so that this surface is mid-distance between the ghost and the image nodes (Fig. 2a). The normal to Γ is defined from the level-set function:

$$\widehat{n} = \frac{\nabla d(\boldsymbol{x_k})}{|\nabla d(\boldsymbol{x_k})|}\,, \tag{3}$$

In the case of corners, the normal is set as the bisector of the angle formed by the two edges, as seen in Fig. 2b.

The value Φ_{IP} is determined in the fluid from linear, bi-linear or tri-linear interpolations. The interpolation stencil depends on the nature of the points bordering IP

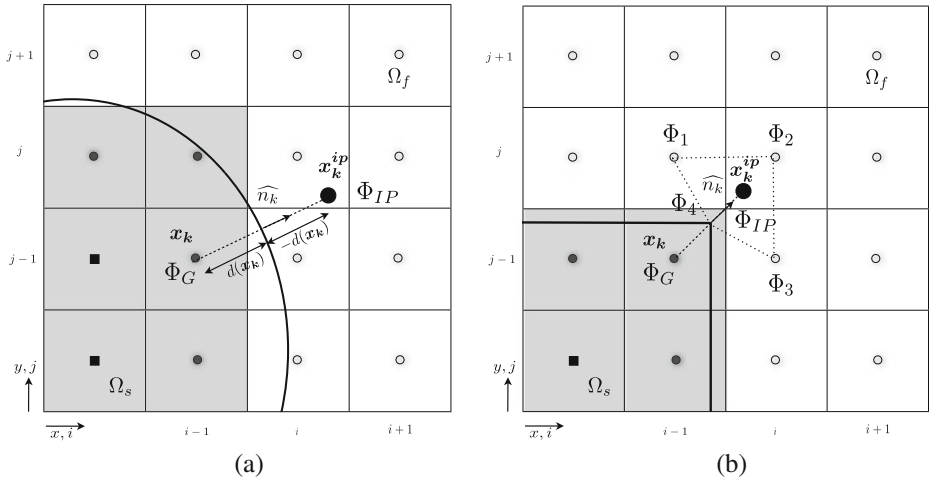

Fig. 2 Definition of the image point (IP) associated to the ghost point (G). *Open circle*: Fluid cell, *Filled square*: Solid cell, *Filled circle*: Ghost cell

and three configurations exist, which are depicted in Fig. 3. It may be the case that the interpolation stencil for a given ghost cell contains one or more ghost cells, then the stencil is modified to replace the ghost points by their normal boundary intercepts, as shown in Fig. 3.

Linear interpolation may be used for boundaries aligned with the Cartesian grid directions. For Γ-surface featuring more complex three-dimensional (resp. two-dimensional) shapes a trilinear (resp. bilinear) interpolation is retained. This may be cast in:

$$\Phi_{IP} = \sum_j \omega_j \Phi_j \tag{4}$$

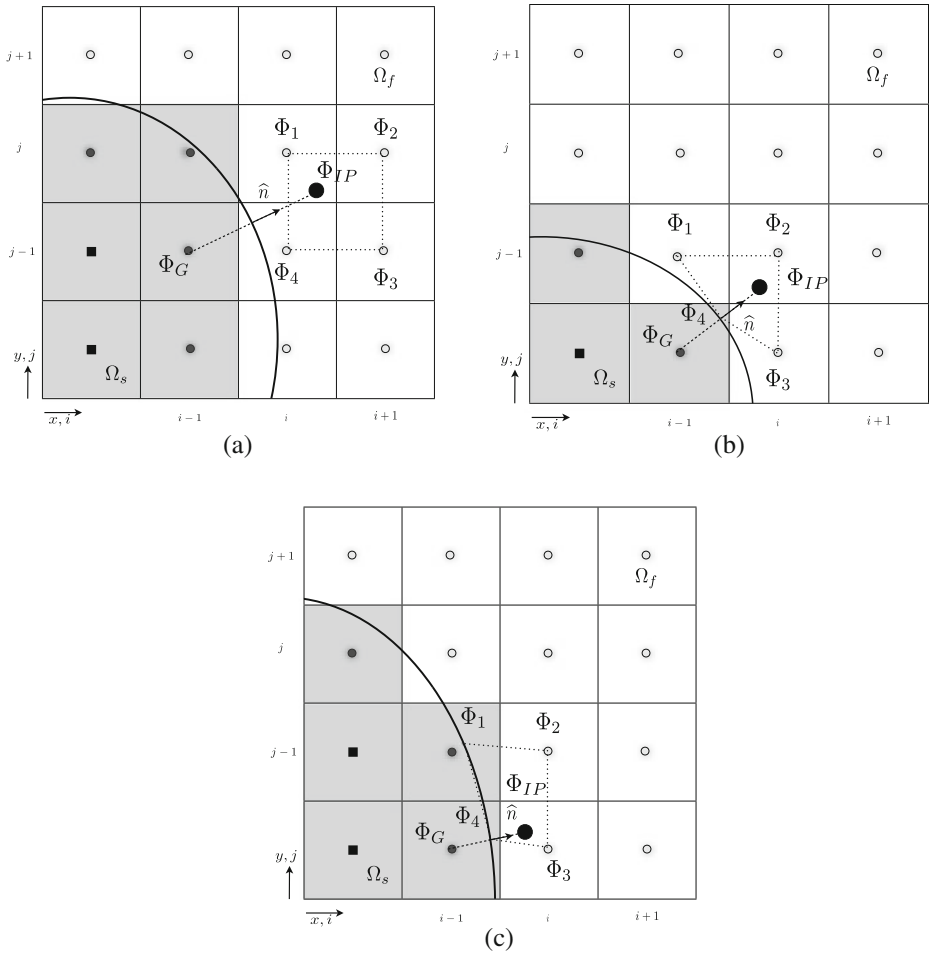

Fig. 3 Schematic of the bilinear interpolation stencil. **a** General case with four fluid cells. **b** One point in the interpolation stencil is the ghost point itself. **c** The interpolation stencil may include other ghost cell. *Open circles* indicate the fluid cells. *Filled circles* mark the nodes whose the solution needs to be reconstructed. *Filled squares* illustrate the solid nodes

with the coefficients $\omega_j = B_{ij}^{-1} x_i$, given from the inverse of the matrix B_{ij} expressed from the interpolation-node coordinates [17].

Conditions of Dirichlet type are prescribed for the velocity, to capture no-slip walls, and of Neumann type for pressure and some scalars; to close the energy equation, the wall temperature is calculated by using an adiabatic hypothesis. To impose these boundary conditions, the flow-field variables at ghost cells are determined from a linear approximation along the normal to the boundary. In the present flow solver, the vector of primitive variables associated to the ghost cell is updated at each sub-step of the third-order Runge Kutta time stepping. The Dirichlet boundary conditions are of second order accuracy while the Neumann boundary conditions provides locally first order, but globally second-order accuracy, as discussed in [47]. To ensure a reasonable wall-flow resolution, the nearest point from the effective boundary should be in the viscous sublayer, thus enabling the use of a linear interpolation for the velocity components. Good accuracy was reported in the literature with a linear interpolation scheme for high Reynolds number flows interacting with complex surfaces [26]. Weaker resolution usually goes with the introduction of a law of the wall in the modeling; then a linear interpolation is inadequate and higher-order interpolation should be used, specifically for the normal component [41] and, in this specific context of law of the wall, modified interpolation schemes were discussed [6].

3.1 A Compressible Conservative Immersed Boundary (CCIB)

When dealing with the ghost cell approach, the continuity equation is not taken into account, which can result in loss or gain of mass. However, for sufficiently refined mesh, it will be shown below that the error on mass conservation stays moderate. Nevertheless, when the proportion of ghost/solid cells inside the computational domain becomes high or in the case of a coarse mesh, the error on mass conservation can be reduced by using a conservative formulation of the immersed boundary method. This section reports an extended version, to fully compressible flows, of the cut cell approach [29, 45], initially developed for constant density flows. Mass conservation is then secured and spurious pressure noise is damped.

The discretized budget of a quantity φ may be cast in:

$$\frac{\partial \hat{\varphi}_{ijk}}{\partial t} = \frac{1}{\mathcal{V}_{ijk}} F_{ijk}[\mathcal{F} + \mathcal{C}], \tag{5}$$

where $\mathcal{V}_{ijk}$ is the cell volume, $\hat{\varphi}$ is the volume average of φ and $F_{ijk}[\mathcal{F} + \mathcal{C}]$ stands for the discretized form of the viscous and convective fluxes.

The numerical scheme is modified in the vicinity of the immersed boundary, to be consistent with the finite volume formulation and preserve the actual solid/fluid volume ratio. In the basic ghost cell approach, the exact shape of the fluid cells near the boundary is not detailed and this may be improved modifying the volume balance in removing the solid subset.

The cut cells are first identified, i.e. the fluid cells with a subset contained in the embedded body, then α_{ijk} is defined as the fluid volume fraction of these cells ($0 \leq \alpha_{ijk} \leq 1$), to estimate the fluid cell volume as $\alpha_{ijk}\mathcal{V}_{ijk}$. The wetted surfaces ($\mathcal{S}_{i-1/2jk}$, $\mathcal{S}_{i+1/2jk}$, $\mathcal{S}_{ij-1/2k}$, $\mathcal{S}_{ij+1/2k}$, $\mathcal{S}_{ijk-1/2}$ and $\mathcal{S}_{ijk+1/2}$, Fig. 4) are determined to integrate the

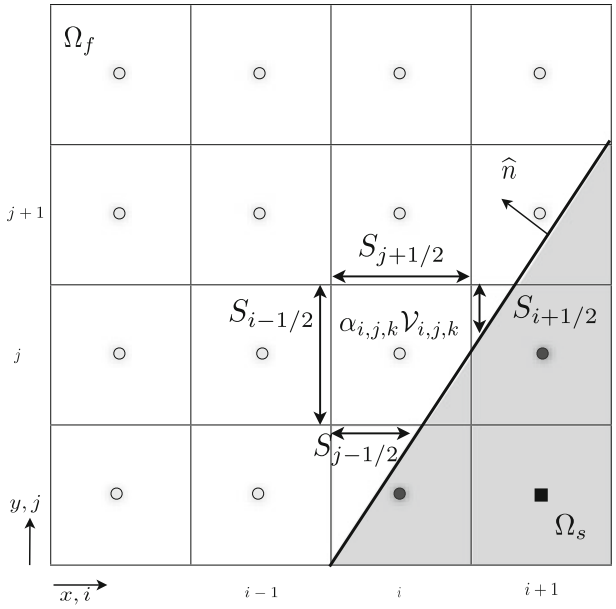

Fig. 4 Treatment of the interface cells: the fluid cells in the vicinity of the embedded surface are balanced with the real fluid volume

convective fluxes over the real wetted surfaces of the control volume $\alpha_{ijk}\mathcal{V}_{ijk}$ [29, 45]. In the simulations reported here, these border convective fluxes are determined with a second-order skew-symmetric-like formulation [12]. To accurately estimate the fluxes for the cut cells, ghost points within the solid domain are still defined as above.

Concerning the viscous numerical fluxes, the cut-cell stencil includes an additional term, $\mathcal{D}_{ijk}$, representative of the friction force at the immersed wall and that was neglected in Eq. 5:

$$\mathcal{D}_{ijk} = -\int_{\Gamma_{ijk}} \boldsymbol{\tau} dS. \tag{6}$$

where Γ_{ijk} is defined as in Fig. 5. For an immersed wall and for an incompressible case, as discussed in [45], velocity gradients in wall tangential directions are assumed weak, so that the wall shear stress becomes:

$$\tau = \mu\left(\frac{\partial u_{||}}{\partial x_n}\right) \tag{7}$$

with $u_{||}$ the flow velocity parallel to the wall and x_n the normal distance to the wall. The friction force may then be determined from interpolation, to project it along the cartesian mesh directions [45].

Undesirable pressure noise was found to be reduced in our fully compressible simulations, if the viscous fluxes are not pondered by the effective wetted surface, but readily estimated from the ghost cell. The viscous fluxes along the immersed wall are then specified as the linear average of the viscous fluxes on the solid subset of

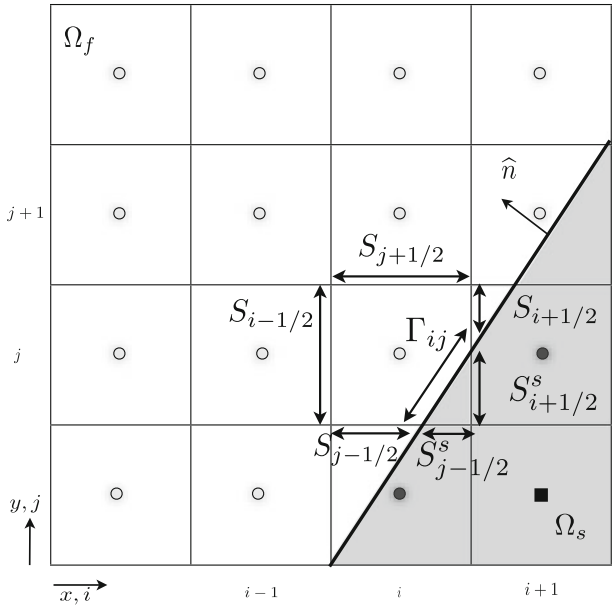

Fig. 5 Treatment of the interface viscous fluxes for a cut-cell

the planes delimiting the control volume $\mathcal{V}_{ijk}$, multiplied by the immersed section, as shown in Fig. 5, leading to:

$$\mathcal{D}_{ijk} = \frac{1}{2}\Gamma_{ijk}(\mathcal{F}_{i+1/2\,jk} + \mathcal{F}_{j-1/2\,jk}), \tag{8}$$

where $(\mathcal{F}_{i+1/2\,jk} + \mathcal{F}_{j-1/2\,jk})$ is the linear average friction, obtained from the viscous flux. The numerical stencil for the cut cells may thus be written as:

$$\frac{\partial \hat{\varphi}_{ijk}}{\partial t} = \frac{1}{\alpha_{ijk}\mathcal{V}_{ijk}}\left(F_{ijk}[\mathcal{F}+\mathcal{C}] + \mathcal{D}_{ijk}\right). \tag{9}$$

To prevent the appearance of very small cells, which can result in numerical instability, the cell mixing procedure [25, 29, 45] is used for the cut cells; overall this method consists of mixing small cells with their neighboring ones. To find the proper target cells to be mixed, mixing directions and fractions are determined, involving the normal vector components. As shown in Fig. 6, a ghost cell (i,j,k) with a fluid subset $\alpha_{ijk}\mathcal{V}_{ijk}$ has three target cells in two dimensions. The first target cell is identified in the x-direction as the cell located in $(i+1,\ j,\ k)$ or $(i-1,\ j,\ k)$ according to the sign of the x-component of the normal $\boldsymbol{n}_{ijk}$, and the same is done in other directions and also along the diagonal.

3.2 LES-immersed boundary coupling

Specific difficulties arising with immersed boundaries in the context of Large Eddy Simulation have been addressed at many places in the literature [1, 13, 24, 26, 28, 65, 66]; the most stringent ones relate to the filtering operation in the vicinity of walls, therefore close to ghost cells. In the present work, Large Eddy simulations have been carried out with various subgrid scale strategies, some requiring explicit filtering.

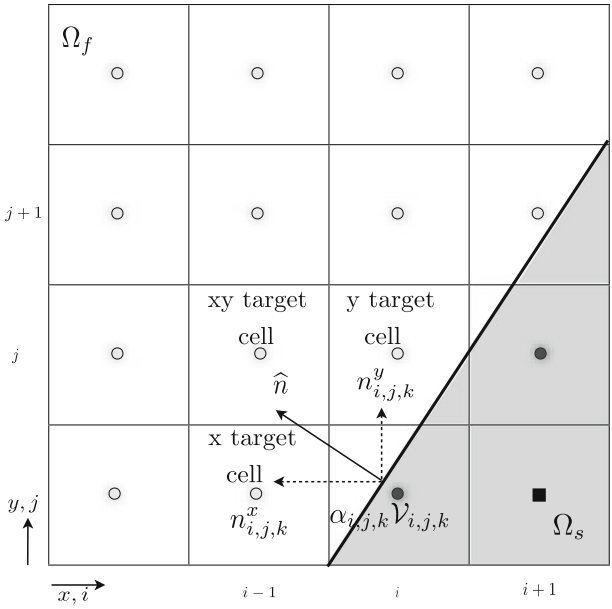

Fig. 6 Shematic of the mixing procedure for a ghost cell with a small fluid subset

To determine the dynamic coefficients appearing in the eddy-viscosity models, the resolved fields are filtered using a discrete top-hat filter of characteristic width 2Δ, with Δ the implicit grid filter. This test filter is described by a trapezoidal rule [72], generalized for non-uniform grids [39]. This operation should be modified in the near-wall region to prevent the inclusion of solid points in the discrete filter. The filtered quantities near the immersed boundaries are then determined by cutting the filtering volume. In other words, the scheme is switched to bi-dimensional filtering

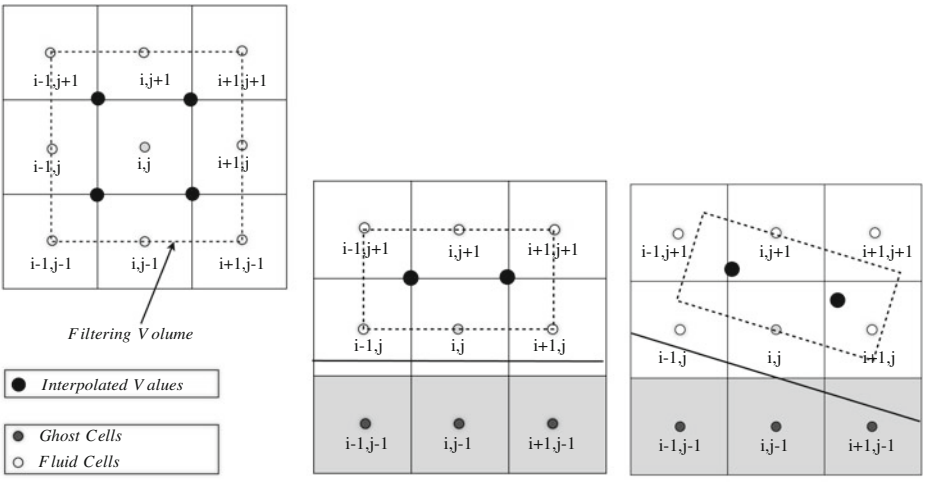

Fig. 7 Explicit Filtering volume in two dimensions. **a** In the fluid region. **b** Near an horizontal immersed wall. **c** Near an inclined immersed wall

over the plane parallel to the immersed boundary (Fig. 7). This operation may nevertheless leads to commutation errors since the filter becomes anisotropic. In a similar manner, the Lagrangian reconstruction of the fluid path in the Lagrangian Subgrid Scale Dynamic model [44] is modified in the vicinity of immersed boundaries.

4 Testing Immersed Boundaries

In this section, the prediction capabilities of immersed boundaries in compressible flows are estimated considering various canonical test cases, as pressure reflection over oblique surfaces, mass conservation in a channel flow past a cylinder and inclined channels. Then, simulations are compared against experimental results for the flow past a square obstacle, before considering a transonic flow cavity in the subsequent section.

4.1 Pressure-wave reflection

The similarities and differences between characteristic boundary conditions based on traveling waves (as NSCBC [54]) and the Neumann (zero pressure gradient) combined to a Dirichlet (imposed velocity) condition at walls, have been studied in [33] for grid conforming to the shape of the body. However, the impact of an immersed boundary reconstruction with the wall that does not coincide exactly with the grid mesh, needs to be assessed also. In this section, the response of a spherical pressure wave interacting with a wall boundary is examined using both the 3D-NSCBC formalism [38] with a conforming grid, and, immersed boundary with a non-conforming grid. In practice, the two techniques prescribe the same wall acoustic-impedance that goes to infinity; the differences arise from the numerically point of view, in the sense that 3D-NSCBC is an indirect and smooth imposition of the boundary conditions, which allows some relaxation of the variables towards target values.

A Gaussian-shaped pressure pulse is imposed at the center of a three-dimensional box of side length $L = 0.013$ m:

$$p(r) = p_\infty \left[1 + \delta \exp\left(-\frac{r^2}{2R_p^2} \right) \right] \tag{10}$$

where $r = \sqrt{x_1^2 + x_2^2 + x_3^3}$ is the distance from the center of the computational domain, R_p is the characteristic dimension of the pressure pulse ($R_p = 0.05L$), $\delta = 0.001$ is its amplitude, with $T_0 = 300$ K and $p_\infty = 1 \cdot 10^5$ Pa. A uniform mesh composed of 50 nodes in every direction is used.

With immersed boundaries, near the wall the pressure wave relies on interpolations. Faces and edges are determined from a bilinear interpolation and corners reconstruction depends on a tri-linear scheme, whose actual impact on flow physics varies with the angle between the cartesian mesh and the immersed body. Results from the two boundary treatments are shown in Figs. 8 and 9 for acoustic reflexion including a 45° inclined box. The immersed boundary formalism reproduces the pressure waves observed with 3D-NSCBC, without much spurious oscillations and

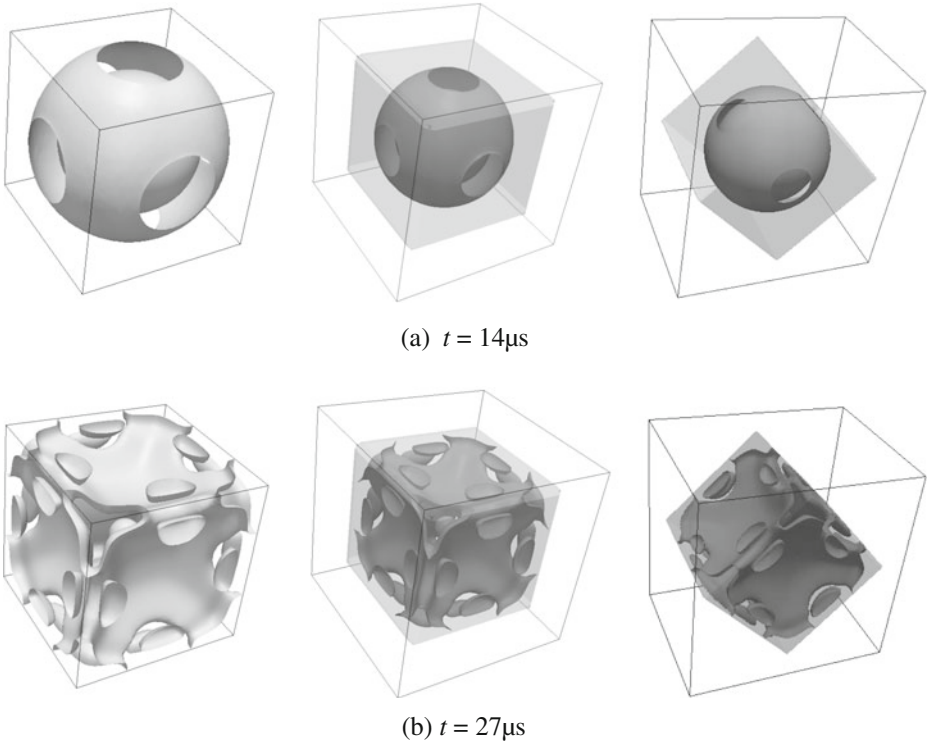

Fig. 8 Pressure iso-surfaces. *Left*: 3D-NSCBC wall formulation. *Center*: Immersed boundaries with walls parallel to mesh. *Right*: with a 45° inclined cube

noise, as confirmed when comparing the time evolution of the pressure signal at points located on one edge, corner and center of a face (Fig. 10). The agreement between the three test cases is almost perfect, except in the case of the 45° inclined cube, where some moderate departure is observed in the center of the cube face.

To calibrate the impact of immersed boundaries on the numerical scheme's accuracy when approaching the wall, additional simulations were performed with a resolution varying between 40 and 70 fluid nodes in every direction, with a conforming grid and immersed boundaries, in the case of the 45° inclined box. Two probes are located either in the center of a face or in a corner, to collect the pressure time evolution. These signals are then compared against a reference conforming mesh solution obtained with a 150 fluid nodes resolution. L1 and L2 norms are computed for a pressure wave traveling over 30 t_r, where t_r is defined as in Fig. 10. For both 3D-NSCBC (conforming wall) and IBM, the discretization at wall is found to be close to second order, as seen in Fig. 11.

4.2 Mass conservation: flow past a confined cylinder

The ghost cell technique enforces the boundary condition on the immersed body through the use of an interpolation scheme, which combines wall information with

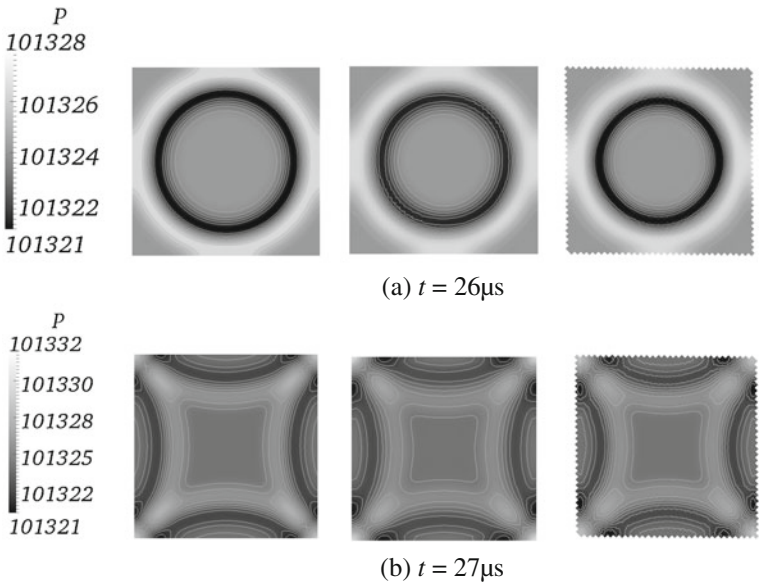

Fig. 9 Pressure map and pressure contours at two different times. *Left*: 3D-NSCBC wall formulation. *Center*: Immersed boundaries with walls parallel to mesh. *Right*: with a 45° inclined cube

the nearest fluid cells. Because the primitive variables are interpolated without regard to the finite volume integration, fundamental conservations laws are not explicitly enforced in the near wall cells. To evaluate the consequence of such an interpolation scheme, a circular cylinder placed inside a channel flow is investigated with two-dimensional simulations, to measure the level of mass conservation error introduced by immersed boundaries in compressible flows.[1]

A flow configuration previously examined in the literature is retained [7, 70], where a circular cylinder of diameter d is in a channel flow of height $h = 5d$. To prevent spurious wave reflections, the cylinder is located half-way up and three channel heights away from the inlet plane, the simulations are with a non-uniform grid of 200×82 nodes in longitudinal and spanwise directions, the 1 mm cylinder is discretized over 70 ghost cells. The bottom and top boundaries are adiabatic no-slip walls and the open inflow and outflow boundaries are subsonic non-reflecting [38]. At inlet, a small asymmetric perturbation is superimposed to the velocity profile for a short time to initiate the vortex shedding, as in [70]. The critical Reynolds number, $Re_d = 232$, at which vortex shedding appears is reproduced.

To calibrate the error on mass conservation in this unsteady simulation, mass-budget control volumes are cumulated over twice a flow characteristic-time $\tau = d/U_o$, with U_o the bulk velocity. The deviation from the exact mass conservation is expected to increase when decreasing the fluid/solid volume ratio, also various volumes have been considered; moving inlet and outlet of the control volume away

[1]Notice that the mass conservation problem arises very differently in incompressible flow solvers, in which mass conservation is mostly a constraint imposed to the velocity solution.

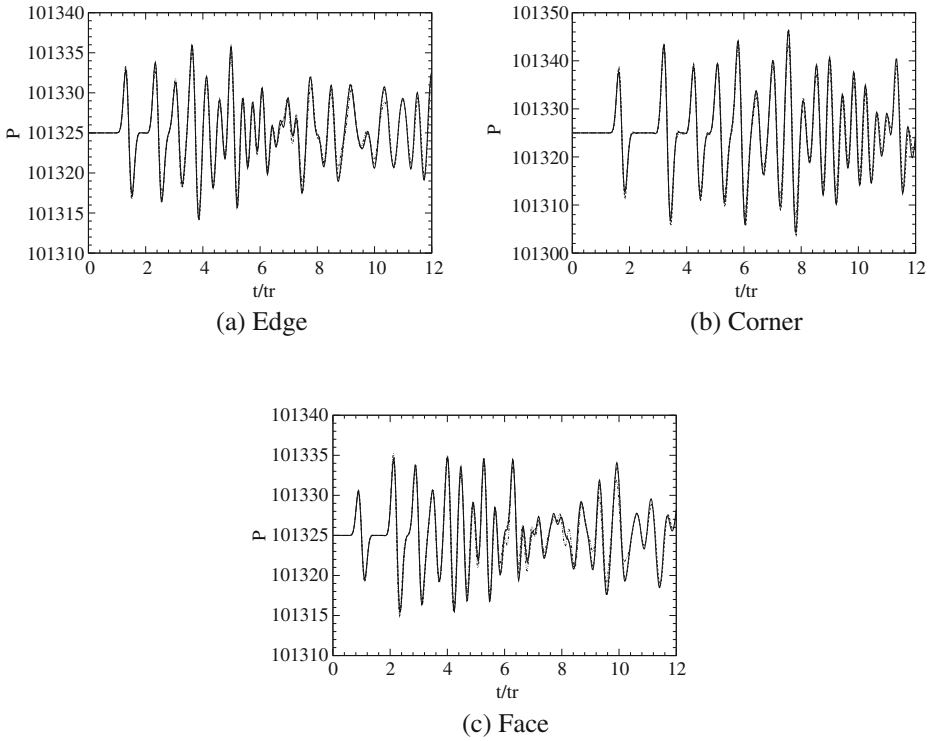

Fig. 10 Pressure signal vs time normalized by the ratio of edge length to twice the sound speed. *Line*: 3D-NSCBC, *Dash-line*: Immersed boundary, *Dotted-dash*: Immersed boundary with a 45° inclined cube

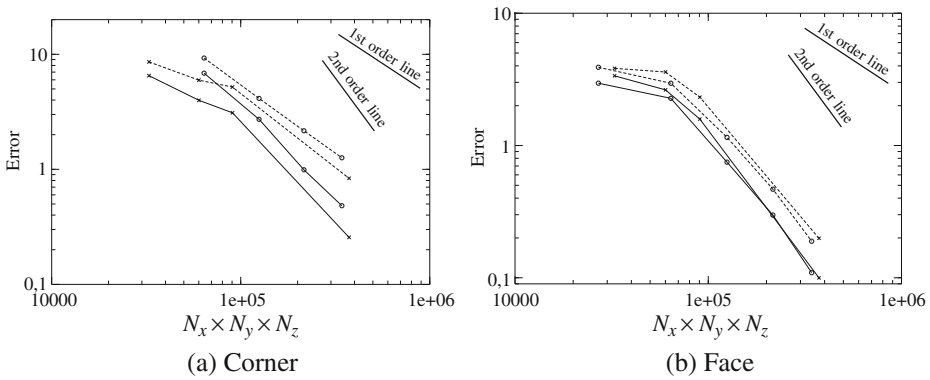

Fig. 11 Evolution of the pressure error versus the number of fluid cells, as defined with L1 (*line*) and L2 (*dashed*) norms. *Circle*: Conforming mesh (3D-NSCBC). *Cross*: Immersed boundaries

from the cylinder, the fluid/solid volume increases (Fig. 12). The mass-conservation error is defined as:

$$\Delta M(t) = \frac{1}{M(t)} \left| M(t) - M(t-\tau) + \int_{t-\tau}^{t} \left(\dot{Q}_m(x_{\max}) - \dot{Q}_m(x_{\min}) \right) dt \right| \tag{11}$$

where $M(t)$ is the mass of fluid in the control volume at time t and $Q_m(x_{\min})$ (resp. $Q_m(x_{\max})$) is the absolute value of the mass flow rate at the inlet (resp. outlet) plane of that volume.

The evolution versus the fluid/solid ratio of the relative error on mass conservation ΔM is measured in %; for every control volume, with and without the cylinder. Without the cylinder, the compressible flow solver ensures mass conservation within 0.01 % of error. With the solid obstacle and for a fluid/solid ratio between 13 and 35, the mass deviation varies between 0.24 % and 0.08 %; it would therefore stay very moderate for most practical simulations, overall below a few thousandths.

Once mass conservation evaluated, Strouhal and drag numbers predictions are compared against previous two-dimensional simulations of the same flow [70] (the experimental values cannot be reproduced with this oversimplifed test case neglecting the spanwise direction [46]). The Reynolds number is increased up to $Re_d = 300$ and the grid is $20d$ and $10d$ in longitudinal and spanwise directions. To test the interpolation scheme, a not very refined 162×100 non-uniform mesh is used ($0.035 < \Delta x/d < 1.5, 0.045 < \Delta y/d < 0.1$). Figure 13 shows the time evolution of drag and lift coefficients. The mean drag coefficient takes the value $C_D = 1.37$ and the Strouhal number, $S_t = fd/U_o = 0.21$, where f is the characteristic shedding frequency; these values are in agreement with previously reported two-dimensional simulations [70].

4.3 Inclined channel at various angles

A laminar Poiseuille flow simulation is analyzed in this section. Varying the flow resolution and the inclination in the cartesian mesh, computations are first performed using the standard Ghost Fluid approach, then the impact on mass conservation of the adjustments proposed in Section 3.1 (CCIB) is quantified.

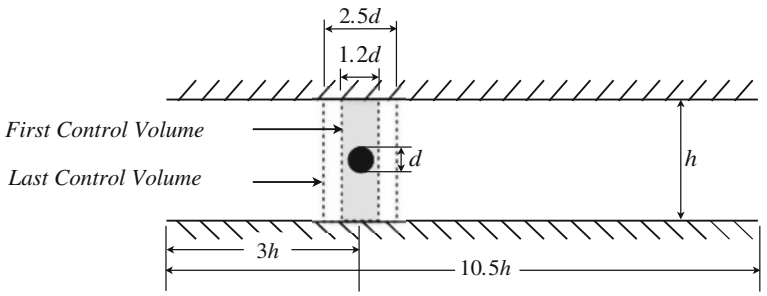

Fig. 12 Sketch of the 2D flow pass a cylinder mass conservation test-case

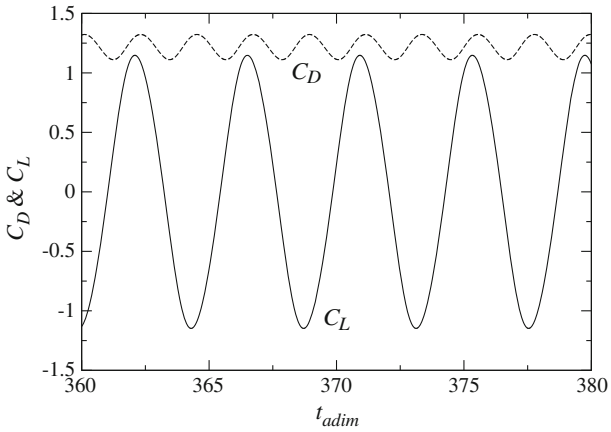

Fig. 13 Time evolution of drag and lift coefficients. 2D flow past a circular cylinder $Re_d = 300$

The generic Poiseuille flow setup discussed in [54] is retained; the Reynolds number based on the half-width channel is $Re_h = 15$ and the inlet flow condition reads:

$$\begin{aligned} u(0, y) &= U_o F(y) \cos(\beta) \\ v(0, y) &= U_o F(y) \sin(\beta) \\ T(0, y) &= T_o \end{aligned} \tag{12}$$

with $0 < y < 2h$ and $F(y) = \cos(\pi(y/h - 1)/2)^2$; U_o is the inlet maximum speed, $T_o = 298.15$ K is the initial temperature, leading to a Mach number of 0.1, and β is the flow inclination in the mesh (Fig. 14). The inlet profile imposes the mass flow rate, however $F(y)$ is expected to evolve toward the exact distribution [54, 59]:

$$F(y) = \frac{3}{4\mu} \frac{1}{Re_h} \frac{\rho_o U_o}{h} y\,(2h - y) \tag{13}$$

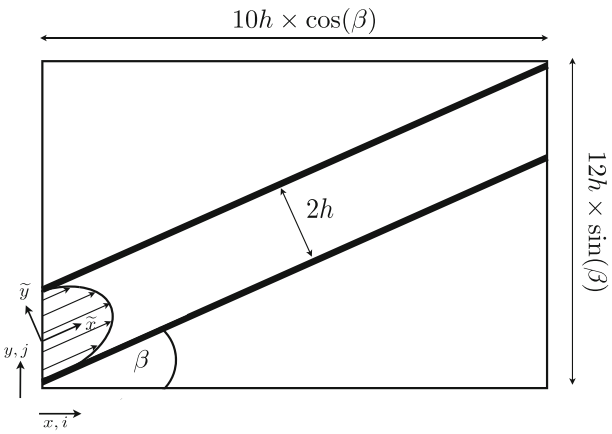

Fig. 14 Computational setup for the channel flow study

Table 1 Grid parameters

Grid	N_0	N_{20}	N_{30}	N_{45}	Number of cells
A	–	9	–	–	30 × 30
B	–	12	–	–	40 × 40
C	52	22	–	–	60 × 60
D	78	32	–	–	90 × 90
E	102	42	34	26	120 × 120
F	–	72	–	–	200 × 200
G	130	–	–	–	150 × 150
H	158	–	–	–	180 × 180
I	–	92	–	–	300 × 300
J	–	142	–	–	400 × 400

N_β is the actual number of grid points in the transverse flow direction for the angle β

The channel length is ten times its half-width (Fig. 14) and the various meshes used are summarized in Table 1, a non-reflecting acoustic boundary is prescribed at the outlet.

Figures 15 and 16 show the impact of both resolution and inclination on the velocity profiles. At 20° of inclination and for various grid resolutions (A, D, E in Table 1), Fig. 15 confirms that the viscous effects of an oblique immersed wall can be captured, with a reasonable sensitivity to resolution; as expected, the results get closer to the theoretical profiles when decreasing the mesh resolution. The same is found in Fig. 16 where the inclination is increased up to 45°, with an under-prediction of the velocity with the coarser grid.

To quantify the error on mass conservation, the absolute mass flow rate deviation between two particular sections is cumulated over 20,000 iterations, for different control volumes and versus N_β, the number of cells over the channel height. The results are shown in Fig. 17 for horizontal and inclined channels at $\beta = 20°$. It is observed that the ghost cell does not induce noticeable gain or loss of mass; for a coarse mesh, at worse the budget is closed at 1 %. Furthermore, the comparison between results obtained for an horizontal channel with a conforming mesh and NSCBC treatment, reveals in Fig. 18 that the mesh-conforming wall boundary-

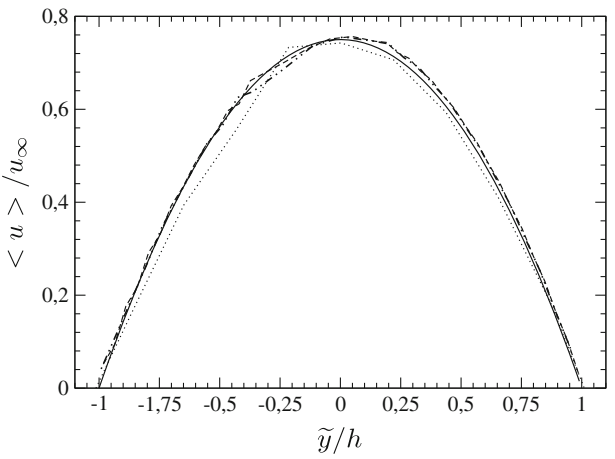

Fig. 15 Streamwise velocity profiles. Inclined channel flow at $\beta = 20°$. *Dotted line*: Grid A. *Dash*: Grid D. *Dot-dash*: Grid E of Table 1. *Solid line*: Analytical solution (Eq. 13)

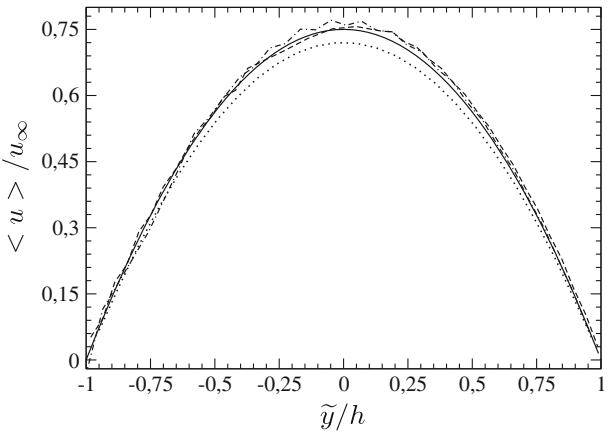

Fig. 16 Streamwise velocity profiles. *Dotted line*: $\beta = 45°$. *Dot-dash*: $\beta = 30°$. *Dash*: $\beta = 20°$. *Solid line*: Analytical solution (Eq. 13)

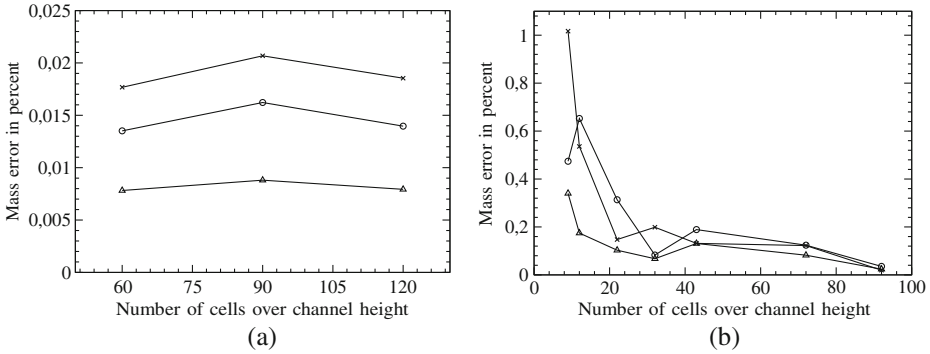

Fig. 17 Mass flow rate deviation in % vs number of cells. **a** $\beta = 0°$. **b** $\beta = 20°$. Control volumes lengths: *Triangles*: $\Delta\widetilde{x} = 2$. *Circle*: $\Delta\widetilde{x} = 3$. *Crosses*: $\Delta\widetilde{x} = 4$ (Fig. 14)

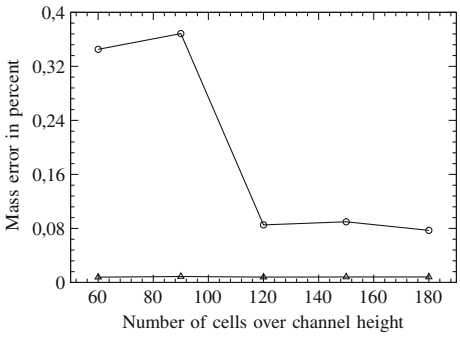

Fig. 18 Mass flow rate deviation in % vs number of cells. *Triangle*: Immersed boundary. *Circle*: NSCBC treatment on conforming mesh

condition produces an extra mass deviation, very likely because of the viscous and convective flux approximation needed in NSCBC. In the case of a mesh-conforming wall, acoustic boundary conditions therefore do not appear as the best compromise; instead, directly imposing a Dirichlet condition for velocity and Neuman for temperature allows for strict mass conservation.

The standard Ghost Cell Method and the CCIB strategy discussed in Section 3.1 are now compared in terms of mass flow rate deviation. There is a significant improvement with the CCIB approach for coarse meshes, increasing mesh resolution brings both methods to the same error level (Fig. 19). In the following, in particular in the case of the cavity flow, the resolution is sufficiently high to allow for using the standard Ghost Cell Method.

4.4 LES of the flow past a rectangular cylinder

After examining laminar flow cases, a three-dimensional turbulent flow past a square cylinder is simulated. The flow considered has been studied experimentally [40, 43] and it features a Reynolds number of 22,000, based on the obstacle side dimension d and bulk velocity, for a Mach number of 0.25. Simulation of this canonical problem may be found in the literature using boundary fitted grid [50, 68] and immersed boundaries [23].

The longitudinal, transverse and spanwise lengths of the computational domain are $14d$, $8d$ and $4d$, respectively and these directions are discretized over a $300 \times 186 \times 50$ mesh. The grid is defined to not conform to the shape of the square and immersed boundaries are with adiabatic no-slip walls. According to experiments [40], synthetic turbulence is injected at inlet with 2 % of bulk velocity fluctuations [30], inlet and outlet are prescribed with 3D-NSCBC [38], symmetric and periodic boundary conditions are used in the spanwise and streamwise directions. Transport by unresolved sub-grid scale fluctuations is modeled with the WALE closure [51].

After a transient time necessary to initiate the vortex shedding behind the square, statistics are collected and compared with experimental measurements. Figure 20 displays the averaged and fluctuating velocities for the streamwise and normal components against experimental data on the cylinder and in its wake, demonstrating the robustness of the simulation procedure along with its prediction capabilities, even with sharp corners.

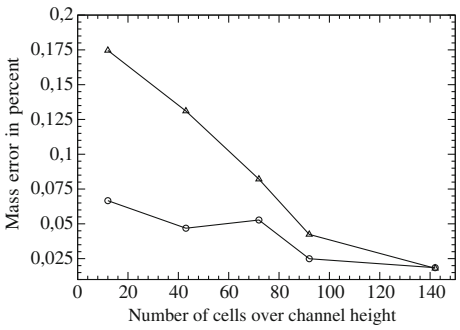

Fig. 19 Mass flow rate deviation in % vs number of cells. $\beta = 20°$. *Triangle*: Ghost Cell Method. *Circle*: Compressible Conservative Immersed Boundary (Section 3.1)

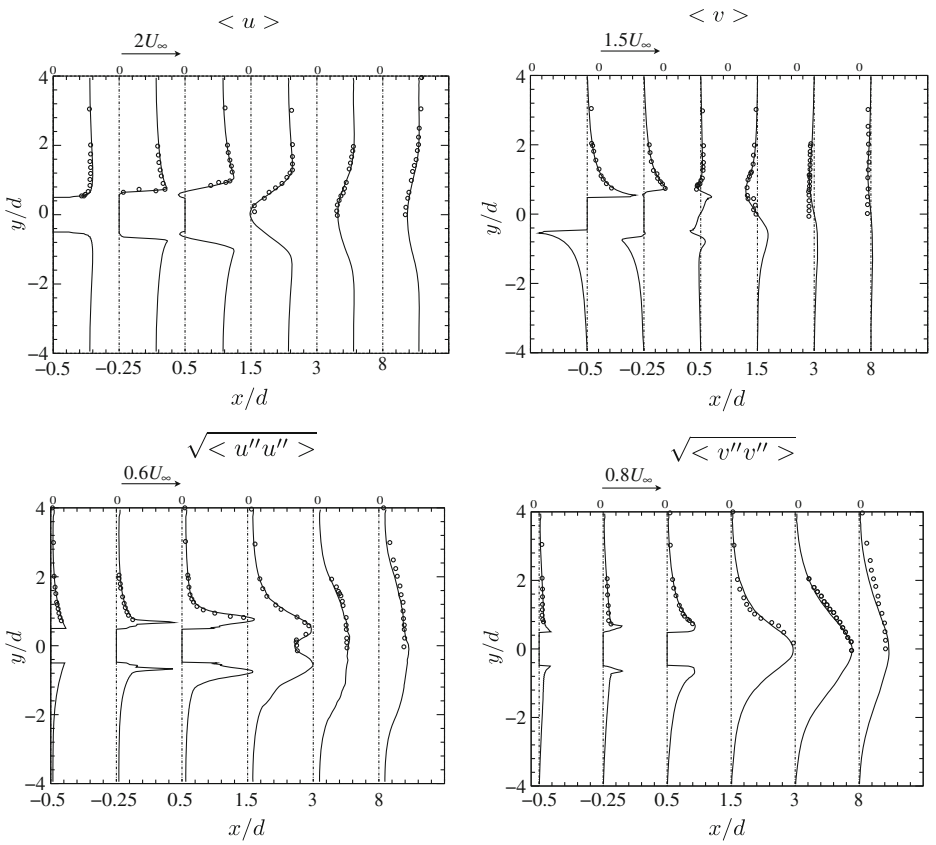

Fig. 20 Time-averaged streamwise and transverse velocity U and V at various longitudinal positions. *Circle*: Experiments. *Line*: LES

5 LES of a Transonic Cavity Flow

To further estimate the prediction capabilities of compressible LES with immersed boundaries in mesh non-conforming to walls, the transonic cavity flow experimentally studied by Forestier et al. [14, 15] is simulated; a configuration already considered with LES in the literature by Larchevêque et al. [37]. Four different sub-grid scale modeling strategies are compared against experimental results and an additional simulation with a multi-block conforming mesh (i.e. without immersed boundaries) is also carried out.

Air flowing at Mach 0.8 encounters a cavity of length-to-depth ratio $L/D = 2$ and spanwise extent $W/D = 4.8$, the Reynolds number based on the cavity length and inflow bulk velocity is $Re_L = 6.8 \cdot 10^6$, the lengths of the three-dimensional computational domain are given in Fig. 21. A flow-acoustic resonance mechanism controls part of the flow dynamics in this experiment [15, 37] where various length-to-depth ratios were examined [14]; hence, the mesh must be refined enough in the vertical direction to capture most of the turbulent boundary layer, but also the mixing layer developing downstream of the cavity. The properties of the two

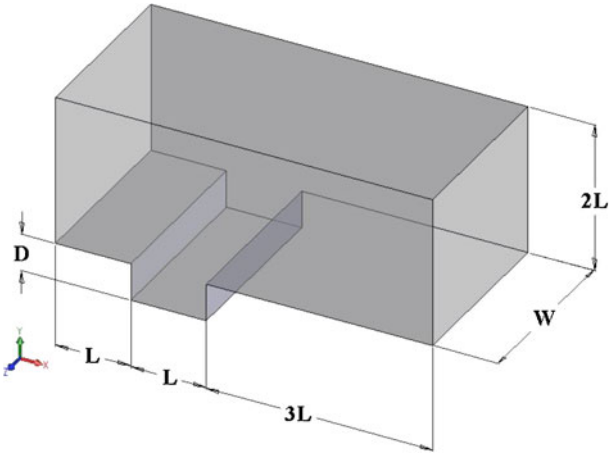

Fig. 21 Sketch of the computational domain

meshes (6.6 million and 30 million nodes) considered are summarized in wall units in Table 2. The signals in the streamwise direction must be sufficiently resolved to propagate most of the acoustic information and an estimation of the boundary layer thickness ($\delta_o \approx 9.79$ mm) was provided by the experimentalist at a longitudinal position located at 0.1 L before the cavity, it is also used to calibrate the mesh in Table 2. The two non-uniform meshes of Table 2 were found to fulfill most of the basic LES resolution requirements. The very regular self-sustained oscillations were experimentally studied using Schlieren technique and the phase-averaged properties of the flow have been collected using a two-component laser-Doppler velocimetry system [15].

Boundary conditions are imposed at inlet, outlet and wall (in the case of the multi-block simulation) using 3D-NSCBC [38]. In addition, as in previous numerical investigation of cavity flows [20, 35–37, 56], the mesh is stretched at the outlet to artificially increase viscosity in order to damp undesired oscillations. With immersed boundaries, the mesh is constructed independently from the wall geometry, which is subsequently arbitrarily imposed on the top of the grid. The flow is forced at inlet with synthetic turbulence [30], but as already concluded [56], intense velocity fluctuations and turbulence are mainly generated by the Kelvin–Helmhotz instability interacting with the flow recirculation within the cavity, therefore the inlet forcing as very little impact on the downstream statistics.

Results with immersed boundaries are first discussed. Figure 22 shows distribution of vortical structures visualized with the Q-criterion; a disturbed large-scale roller

Table 2 Mesh characteristic-length ranges in wall units (denotes by $^+$) and normalized by δ_o, the experimentally reported boundary layer thickness at 0.1 L before the cavity

Mesh	M1	M2
Nodes	$290 \times 188 \times 122$	$514 \times 258 \times 226$
Δx^+	[30, 130]	[4, 30]
Δy^+	[20, 70]	[7, 40]
Δz^+	[20, 50]	[15, 30]
$\Delta x/\delta_o$	[0.04, 0.5]	[0.01, 0.3]
$\Delta y/\delta_o$	[0.002, 0.2]	[0.002, 0.15]
$\Delta z/\delta_o$	[0.06, 0.13]	[0.03, 0.08]

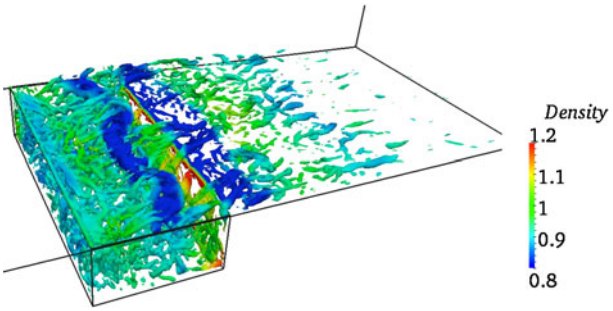

Fig. 22 Snapshot of Q-criterion colored by density. Mesh M1 (Table 2) with Localized Dynamic Smagorinsky modeling [18]

is visible within the cavity, along with the interaction of coherent structures with the downstream cavity-edge, characterized by the impingement on that edge of the detached flow mixed with fluid recirculating within the cavity. A numerical Schlieren view from density gradient is displayed in Fig. 23, the shear-layer oscillations above the cavity are observed, with coherent structures interacting with the downstream edge and pressure waves traveling up- and downstream, above and inside the cavity, featuring strong similarities with what was reported from experiments [15]. It is also seen that LES is sufficiently resolved to capture some of the fine scale flow patterns.

To evaluate the amplitude of compressibility effects, the resolved turbulent Mach number defined as:

$$M_T = \frac{1}{< c >}\left[\frac{\langle\overline{\rho}(\widetilde{\mathbf{u}})^2\rangle}{\langle\overline{\rho}\rangle} - \left(\frac{\langle\overline{\rho}\widetilde{\mathbf{u}}\rangle}{\langle\overline{\rho}\rangle}\right)^2\right]^{1/2} \tag{14}$$

is used, $\langle c\rangle$ is the statistical averaged of the speed of sound. The flow inside the cavity exhibits a compressible field with a resolved turbulent Mach number ranging between 0.2 and 0.3, confirming the compressible character of the flow. In complement to the resolved dynamics, the instantaneous modeling parameter maps for the isotropic and anisotropic parts of the SGS stress tensor have been examined and the so-called Yoshizawa isotropic stress parameter (C_I) may exceed the Smagorinsky one (C_S), indicating similar levels of thermodynamic pressure gradient and SGS kinetic energy. Large values of isotropic stress are found in the vicinity of the pressure waves, while the anisotropic part introduces turbulent viscosity within the cavity, in the shear layers and in the free flow.

Experiments have revealed an asymmetric character of the flow, resulting from a bifurcation induced by the confinement within the lateral walls [37]. This is observed

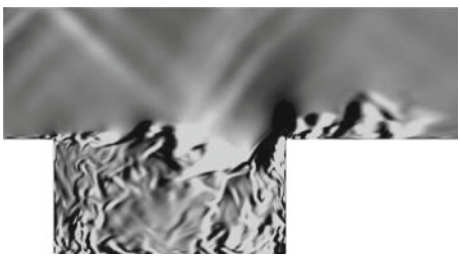

Fig. 23 Numerical Schlieren view. LES mesh M1

in the simulations looking at the horizontal aperture plane above the cavity (Fig. 24); all the SGS modeling approaches feature a non-symmetric flow, with a mean streamwise velocity that is decomposed in a two-core zone developing on the left side of the cavity and a single core on the right side (Fig. 24, left), associated to two

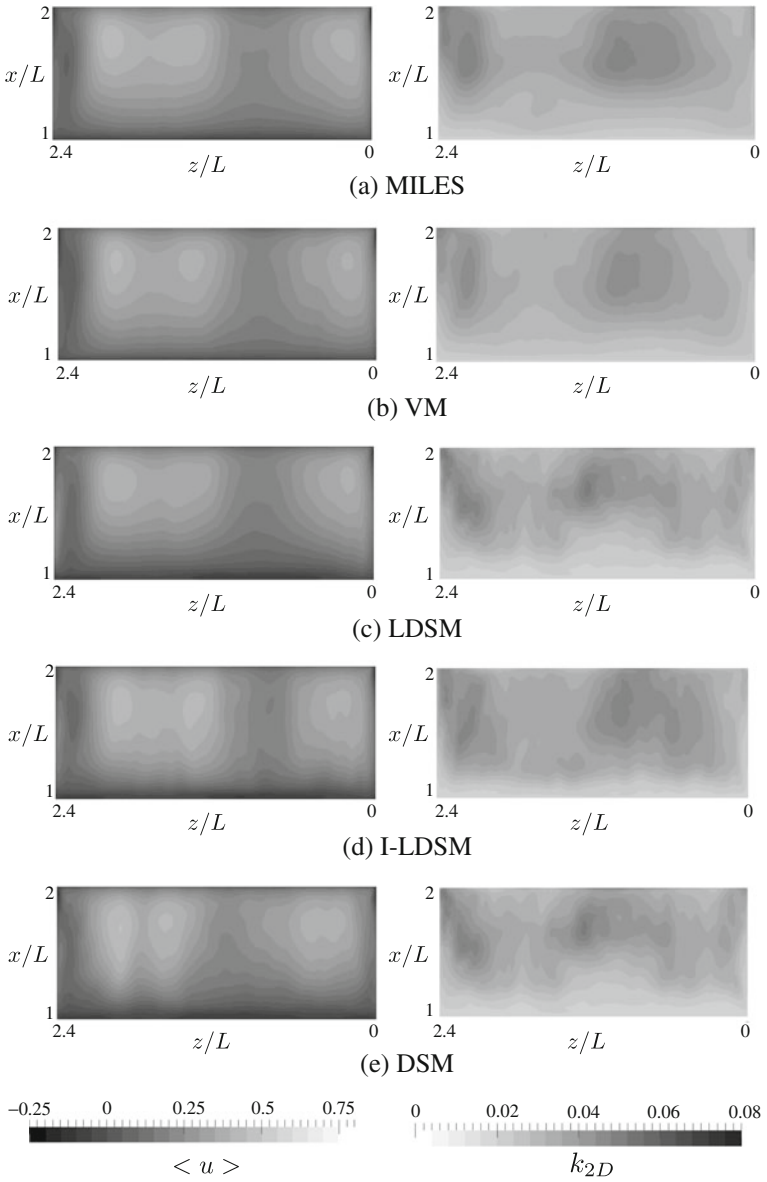

Fig. 24 Maps in the horizontal aperture plane of the cavity. *Left*: time average streamwise velocity. *Right*: Turbulent kinetic energy. **a** MiLES. **b** Vreman et al. model [69]. **c** Lagrangian Dynamic Smagorinsky [44] with macropressure formulation [39]. **d** Lagrangian Dynamic Smagorinsky with isotropic part of the stress tensor [71]. **e** Localized Dynamic Smagorinsky Model [18]

non-centered maximum velocity fluctuations (Fig. 24, right). The MiLES (implicit LES without additional SGS modeling), Vreman et al. [69], Lagrangian Dynamic Smagorinsky [44] with macropressure formulation [39] and with isotropic part of the

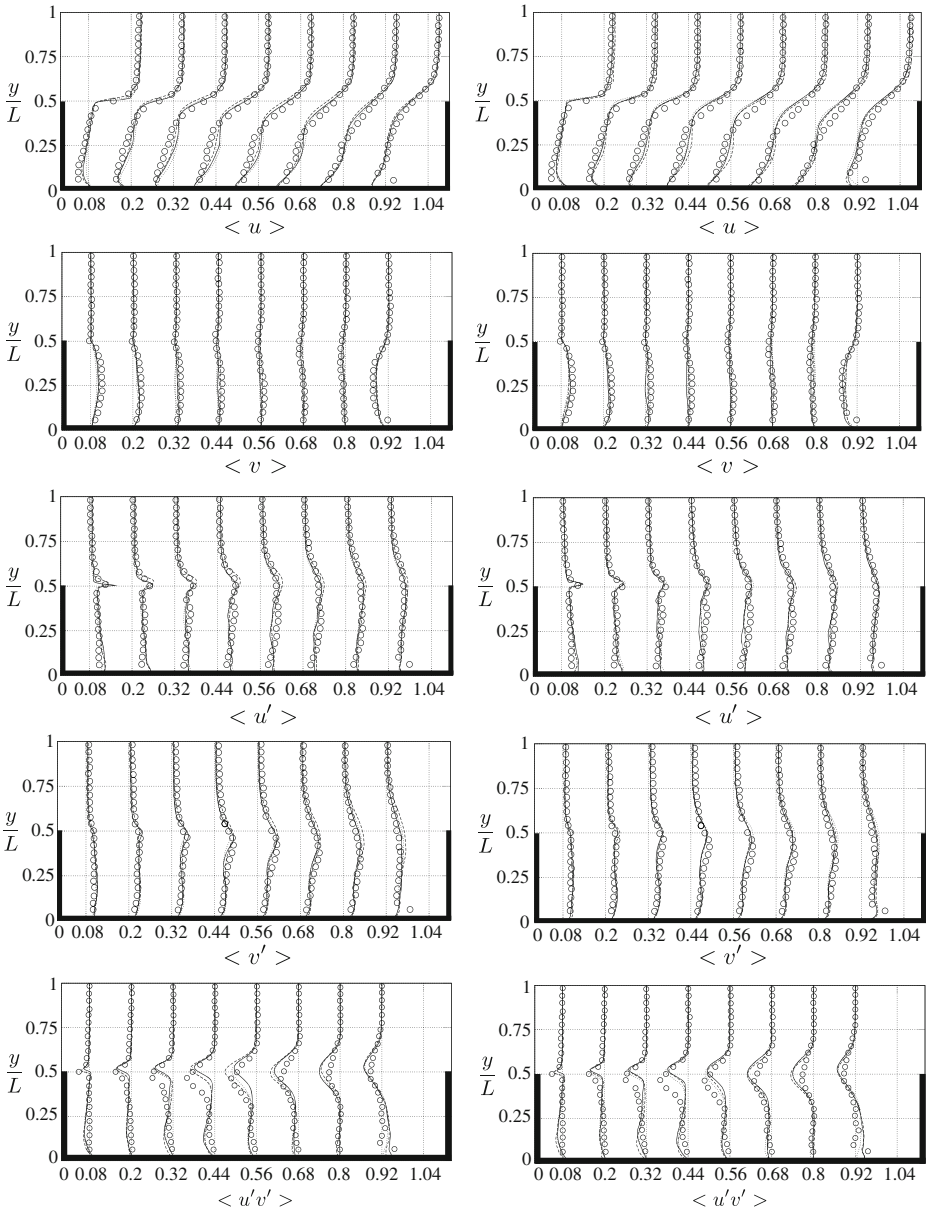

Fig. 25 Velocity statistics in the mid-span plane. Mesh M1 of Table 2. From *top* to *bottom*: Time averaged longitudinal, vertical velocity, longitudinal and vertical fluctuating velocity. *Left*: Wall-conforming mesh. *Right*: Immersed boundaries. *Solid line*: Lagrangian Dynamic Smagorinsky with isotropic part of the stress tensor [71]. *Dotted line*: Vreman et al. model [69]. *Dashed line*: MiLES. *Circles*: Experiments [37]

stress tensor [71] and the Localized Dynamic Smagorinsky Model [18] are compared. They all provide very similar results in terms of amplitude, but the shape of the iso-velocity contours differ, with kernels more or less well-defined and pronounced. Comparison of statistics with measurements is now reported to help discriminate between the modeling approaches.

Figure 25 presents the converged flow statistics for the grid M1 (Table 2), with immersed boundaries and with a wall-conforming mesh using 3D-NSCBC treatment [38], and Fig. 26 for the refined grid M2, also for a wall-conforming mesh. The upper corners of the cavity are very sensitive points in these simulations, they may easily radiate spurious numerical noise [19]; the first conclusion drawn is that the strategies retained here prevent the appearance of these difficulties. Second, there is no significant perturbation or errors induced by immersed boundaries and, in this preliminary global view of the flow statistics, weak differences are observed between the selected SGS closures. Third, refining the mesh from 6.6 million nodes to 30 million, neither profoundly modifies flow statistics nor their agreement with measurements. It is thus concluded that the numerics and the SGS modeling is of sufficient quality to adjust to the mesh resolution. This global comparison may be refined by isolating profiles, as proposed in Figs. 27, 28, 29, 30 and 31.

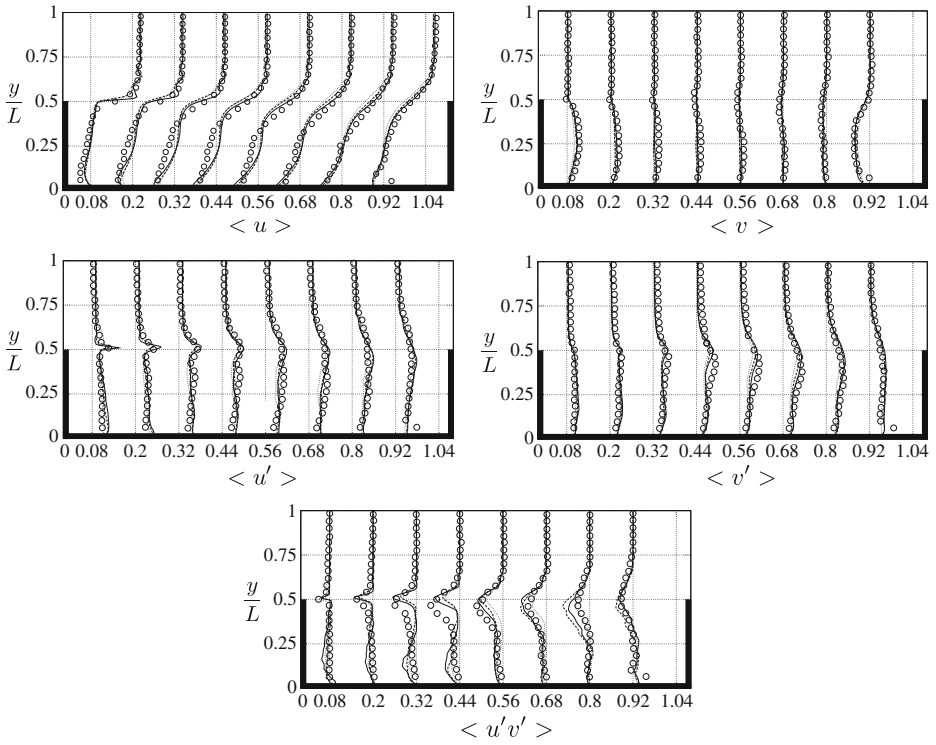

Fig. 26 Velocity statistics in the mid-span plane, wall-conforming mesh (no-immersed boundaries). Mesh M2 of Table 2. From *top* to *bottom*: Time averaged longitudinal, vertical velocity, longitudinal and vertical fluctuating velocity. *Solid line*: Lagrangian Dynamic Smagorinsky with isotropic part of the stress tensor [71]. *Dotted line*: Vreman et al. model [69]. *Dashed line*: MiLES. *Circles*: Experiments [37]

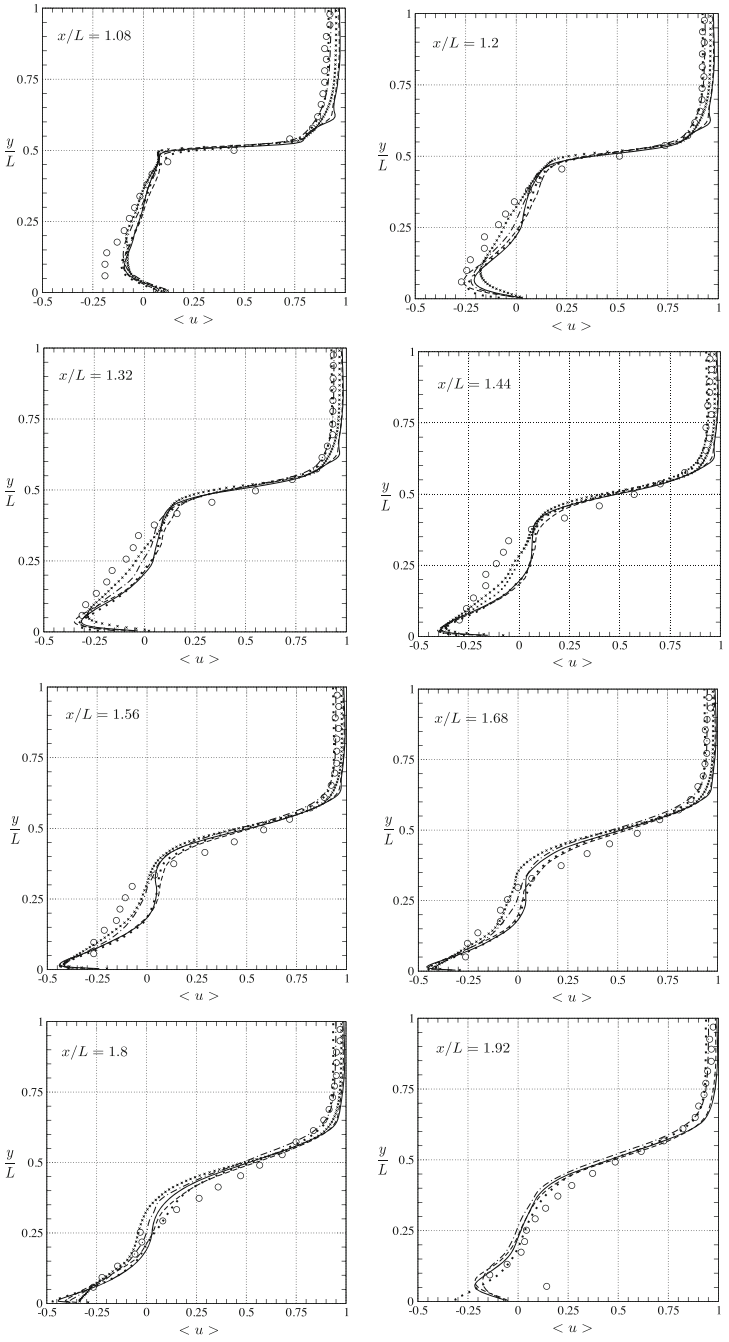

Fig. 27 Time averaged longitudinal velocity in the mid-span plane for different longitudinal positions. Mesh M1 of Table 2. *Solid line*: Lagrangian Dynamic Smagorinsky [44] with isotropic part of the stress tensor [71]. *Dashed line*: Lagrangian Dynamic Smagorinsky with macro-pressure [39]. *Dotted line*: Localized Dynamic Smagorinsky Model [18]. *Crosses*: Vreman et al. model [69]. *Dot-dashed line*: MiLES. *Circles*: Experiments [37] (profiles are positioned in the order of Figs. 25 and 26)

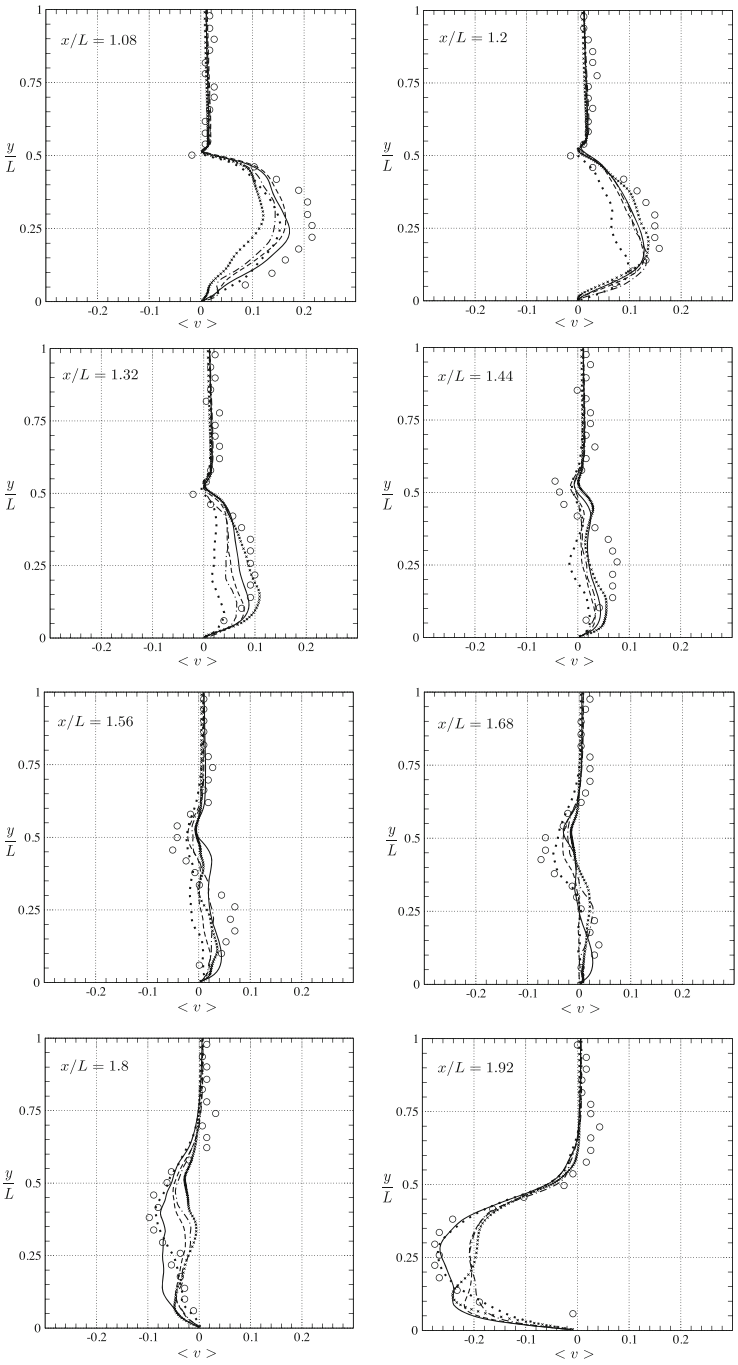

Fig. 28 Time averaged vertical velocity in the mid-span plane for different longitudinal positions. Mesh M1 of Table 2. *Solid line*: Lagrangian Dynamic Smagorinsky [44] with isotropic part of the stress tensor [71]. *Dashed line*: Lagrangian Dynamic Smagorinsky with macro-pressure [39]. *Dotted line*: Localized Dynamic Smagorinsky Model [18]. *Crosses*: Vreman et al. model [69]. *Dot-dashed line*: MiLES. *Circles*: Experiments [37]

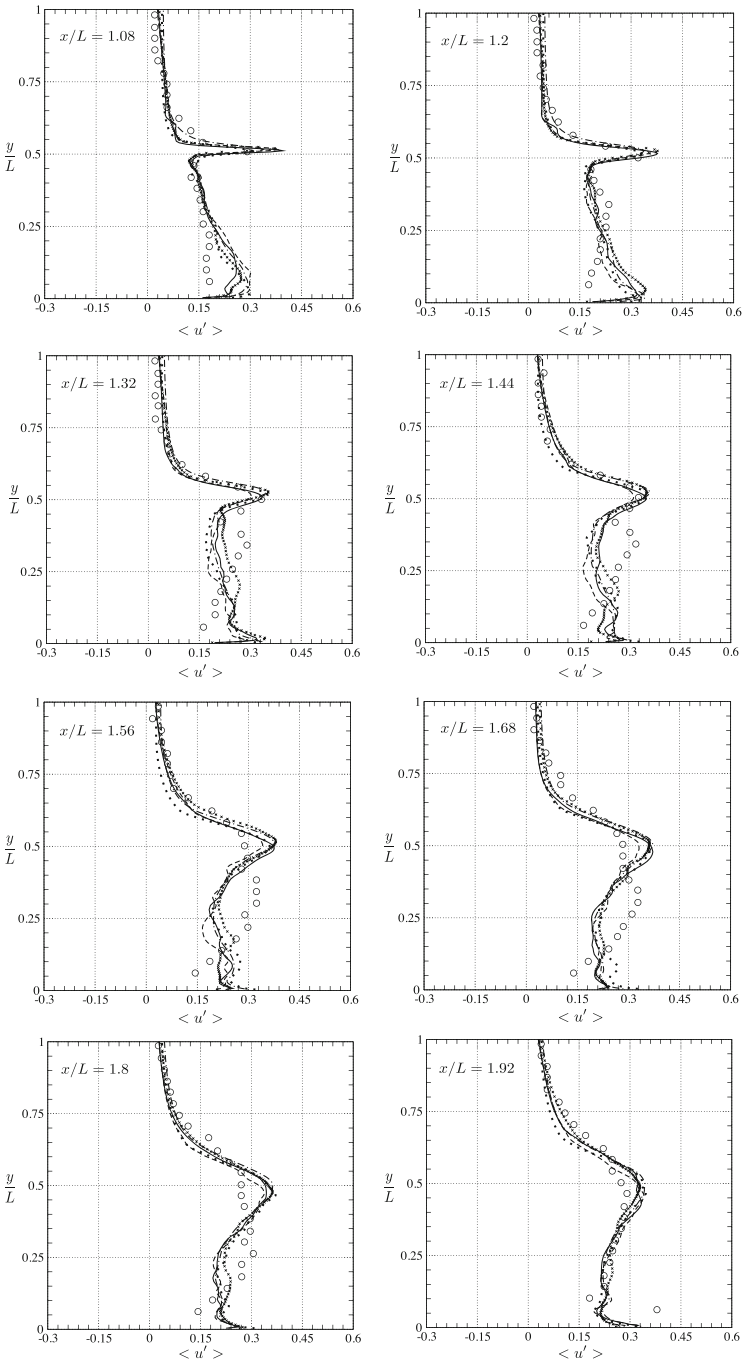

Fig. 29 Time averaged longitudinal velocity fluctuation in the mid-span plane for different longitudinal positions. Mesh M1 of Table 2. *Solid line*: Lagrangian Dynamic Smagorinsky [44] with isotropic part of the stress tensor [71]. *Dashed line*: Lagrangian Dynamic Smagorinsky with macro-pressure [39]. *Dotted line*: Localized Dynamic Smagorinsky Model [18]. *Crosses*: Vreman et al. model [69]. *Dot-dashed line*: MiLES. *Circles*: Experiments [37]

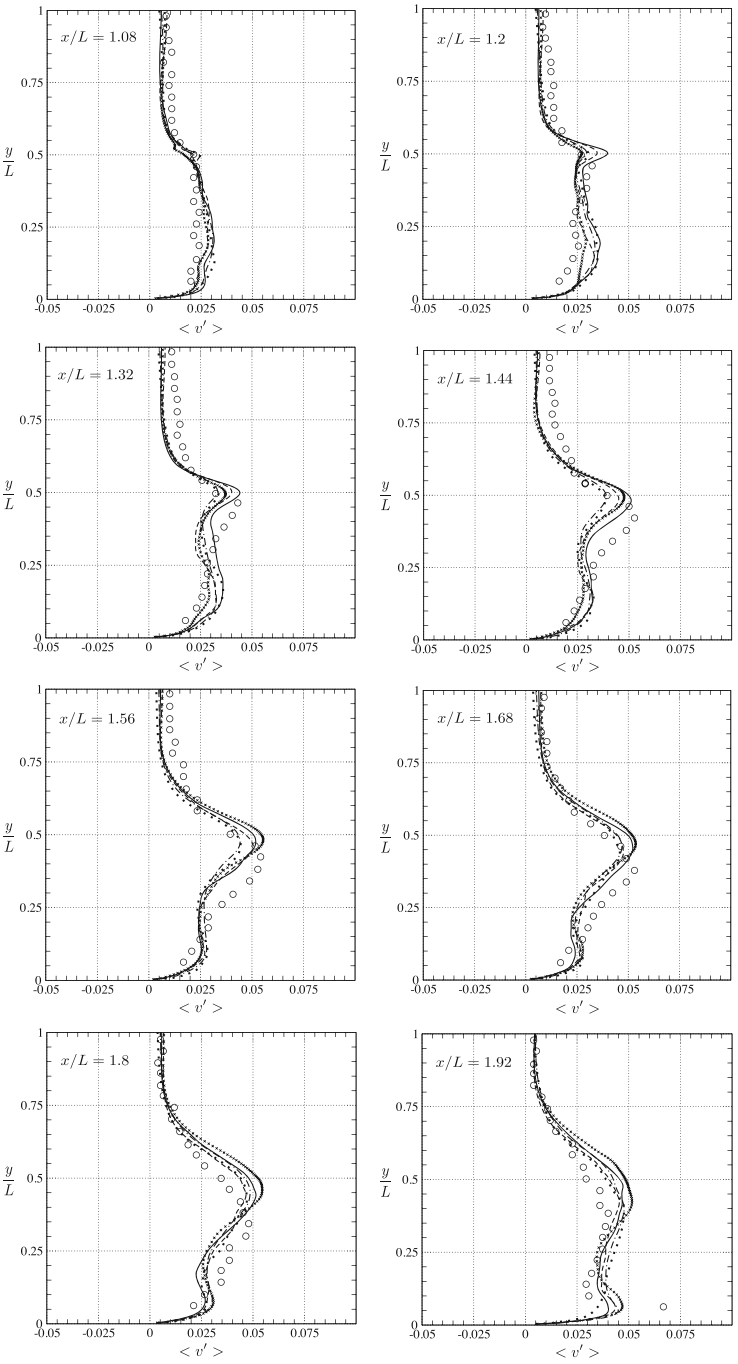

Fig. 30 Time averaged vertical velocity fluctuation in the mid-span plane for different longitudinal positions. Mesh M1 of Table 2. *Solid line*: Lagrangian Dynamic Smagorinsky [44] with isotropic part of the stress tensor [71]. *Dashed line*: Lagrangian Dynamic Smagorinsky with macro-pressure [39]. *Dotted line*: Localized Dynamic Smagorinsky Model [18]. *Crosses*: Vreman et al. model [69]. *Dot-dashed line*: MiLES. *Circles*: Experiments [37]

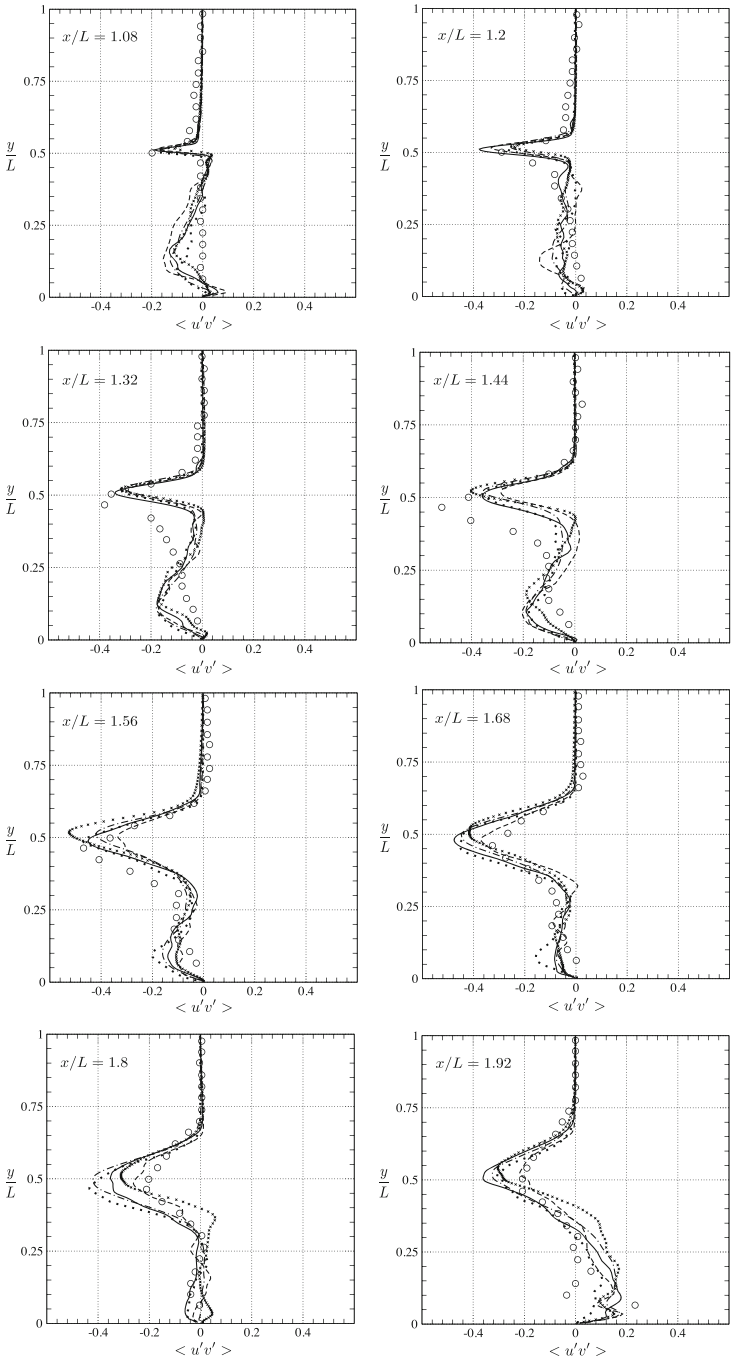

Fig. 31 Reynolds stress in the mid-span plane for different longitudinal positions. Mesh M1 of Table 2. *Solid line*: Lagrangian Dynamic Smagorinsky [44] with isotropic part of the stress tensor [71]. *Dashed line*: Lagrangian Dynamic Smagorinsky with macro-pressure [39]. *Dotted line*: Localized Dynamic Smagorinsky Model [18]. *Crosses*: Vreman et al. model [69]. *Dot-dashed line*: MiLES. *Circles*: Experiments [37]

Looking at details, as reported elsewhere for a deep cavity [64], any small departure on the initial thickness of the upstream boundary layer may explain some of the observed differences. Indeed, when focussing on the first profile ($x/L = 1.08$ in Fig. 27), the boundary layer appears thinner than required. Among all the modeling ingredients, this lack of accuracy in the prediction may be due to the artificial dissipation scheme perturbing the near wall behavior. Within the cavity, the longitudinal mean velocity is also slightly overpredicted and this tendency is reversed in the downstream near wall region. A bump may be observed in the vicinity of $y/L = 0.6$, for $x/L < 1.6$, with Lagrangian Dynamic modeling; the Lagrangian path reconstruction close to the wall along with the specific filtering needed by this closure may be responsible for this behavior. Concerning the vertical velocities presented in Fig. 28, the simulations underpredicts slightly the measured ones; nevertheless, this vertical velocity component brings into play small amplitude compared to the streamwise one.

The fluctuating longitudinal and vertical velocity components are displayed in Figs. 29 and 30 and the longitudinal-vertical Reynolds stress is shown in Fig. 31. The turbulent fluctuation levels are well reproduced near the mixing layer, however inside the cavity, fluctuations are underpredicted (from $x/L = 1.32$ up to $x/L = 1.8$ in Fig. 29). Larchevêque et al. [37] reported similar behavior in their numerical results

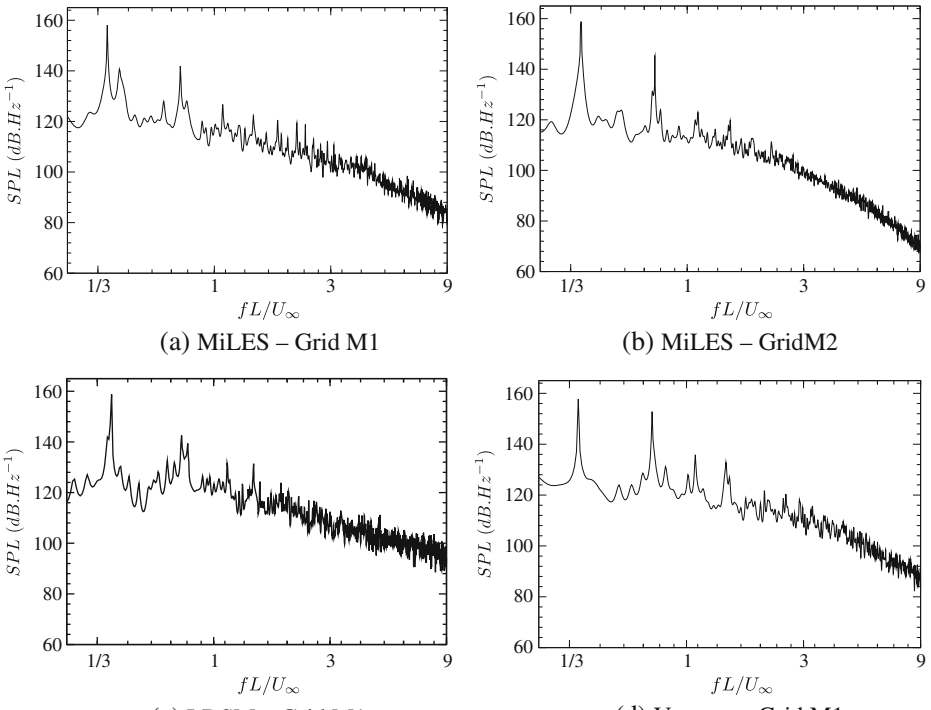

(a) MiLES – Grid M1 (b) MiLES – GridM2

(c) LDSM – Grid M1 (d) Vreman – Grid M1

Fig. 32 Pressure power density spectra. Sensor located in the cavity downstream wall. **a** and **b** No explicit SGS modeling. **c** Localized Dynamic Smagorinsky [18]. **d** Vreman et al. [69]

and relate this discrepancy to the low coherence of the numerical Stuart vortex, which fails to provide the double bumps inside the cavity. Nonetheless, the averaged Reynolds Stresses behavior is quite well captured throughout the cavity (Fig. 31).

A strong acoustic feedback exists in this flow, inducing self-sustained oscillations, previously studied experimentally and numerically [37]. Time pressure signals have been recorded at a point located in the vertical half-span plane on the downstream wall of the cavity. The Power Spectral Density (PSD) is determined for various SGS modeling and for the two grids in the case of the MiLES approach, simulations are with immersed boundaries (negligible differences have been reported in PSD between immersed boundaries and wall-conforming mesh calculations, not shown for brevity). These pressure spectra are plotted (Figs. 32 and 33) in sound pressure level (SPL) in decibels per Hertz versus the Strouhal number, according to:

$$SPL(dB) = 10\log_{10}\left(\frac{S_P}{4\cdot 10^{-10}}\right) \tag{15}$$

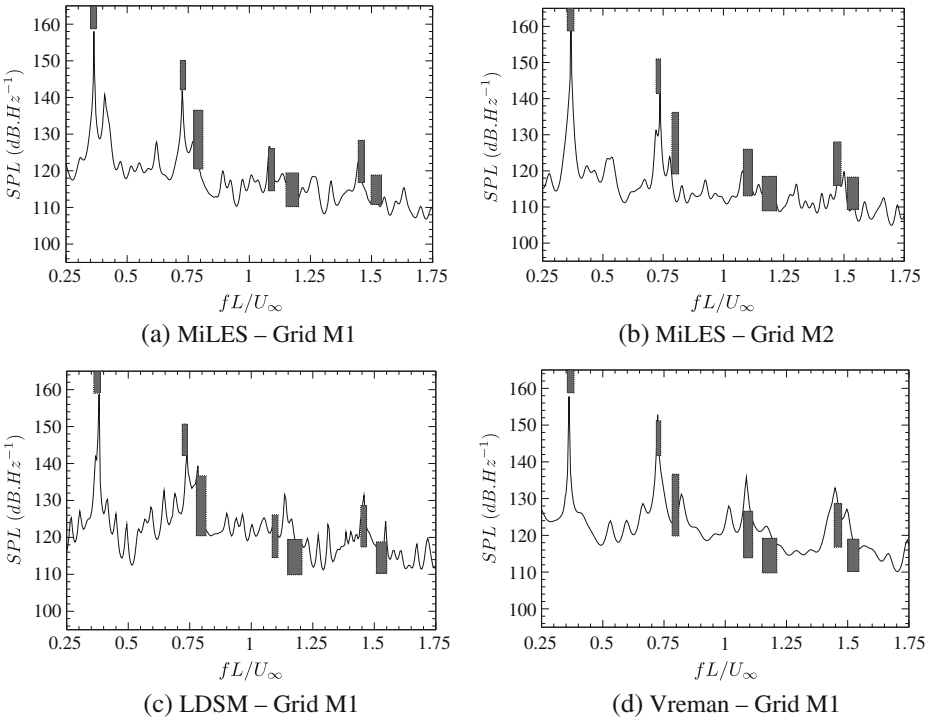

(a) MiLES – Grid M1

(b) MiLES – Grid M2

(c) LDSM – Grid M1

(d) Vreman – Grid M1

Fig. 33 Close up on pressure power density spectra. Sensor located in the cavity downstream wall. **a** and **b** No explicit SGS modeling. **c** Localized Dynamic Smagorinsky [18]. **d** Vreman et al. [69]. *Grey boxes* are experimental ranges (99 % lower and upper boundaries of the density probability functions [37])

where S_P is the spectrum module. The Burg method [4, 42, 57] is used to treat the LES signal, which is known to be more accurate for short sampling; here about 50 periods of the dominant Rossiter mode have been computed, to collect the pressure spectra and statistics. Figure 32 shows the pressure power spectrum and Fig. 33 is a close-up with comparisons against measurements. Best results are obtained with MiLES and Vreman approaches; the Lagrangian Dynamic modeling introduces numerous spurious frequencies, which may result from commutation errors with anisotropic filters, errors cumulated in the averaging procedures along fluid particle trajectories near boundaries. Concerning the Vreman closure, except the first mode and its first harmonics and the second mode, further harmonics of the first Rossiter modes and other modes are clearly over-predicted, suggesting an under-dissipation of these models. However the detailed comparison of fluctuations levels discussed above for the various models, indicates that all closures have difficulties in reproducing the precise levels, with over- or/and under-prediction depending on the exact location examined. In fine, as already concluded in the literature for such transonic flows [37], overall the MiLES approach provides a quite accurate pressure spectrum, with much less spurious harmonics. Moreover, the immersed boundary approach used in the present simulations allows for capturing this unsteady pressure response.

In this cavity flow dominated by pressure oscillations associated to a relatively high turbulent Mach number, the SGS modeling is mainly overwhelmed by the numerical dissipation, thus moderating the relative importance of the subgrid scale closure, as concluded above when comparing with measurements. The magnitude of the molecular, turbulent (SGS modeling) and artificial diffusion fluxes may be extracted from the flow. The SGS and artificial diffusion fluxes are added and compared to the corresponding molecular contribution. Figure 34 shows that the level of artificial viscosity fluxes in the MILES simulation is of the order of the total level of SGS plus artificial fluxes when using Vreman modeling, while the dynamic approach goes with more artificial viscosity. This balance between artificial dissipation and explicit turbulence modeling was discussed in compressible flow literature at many occasions, for instance in the case of shock-interactions studies [11] and shocklets [58]. In terms of spatial distribution of the fluxes added by the SGS closure, the Lagrangian Dynamic approach provides viscosity patterns that follow the flow structure, both at the wall and in the free shear layers featuring traveling acoustic-waves, while the Vreman closure gives a more spotty distribution, without much correlation with flow topology.

The wall-layer is not resolved in these simulations, both with wall-conforming mesh and immersed boundaries. Similar results are obtained in the two cases, suggesting that the interpolation schemes used with immersed boundaries may impact less than artificial viscosity, which actually acts as a wall function when approaching solid boundaries. In the case of subsonic wall-bounded flow, artificial viscosity can certainly be brought down to an almost negligible level of contribution; there the use of wall function may improve the simulation procedure. In the present case of a transonic cavity, featuring quite strong pressure waves, as previously reported in the literature [36, 37], it was not found possible to complete the simulations without a numerical scheme specialized in compressible flows and artificial viscosity.

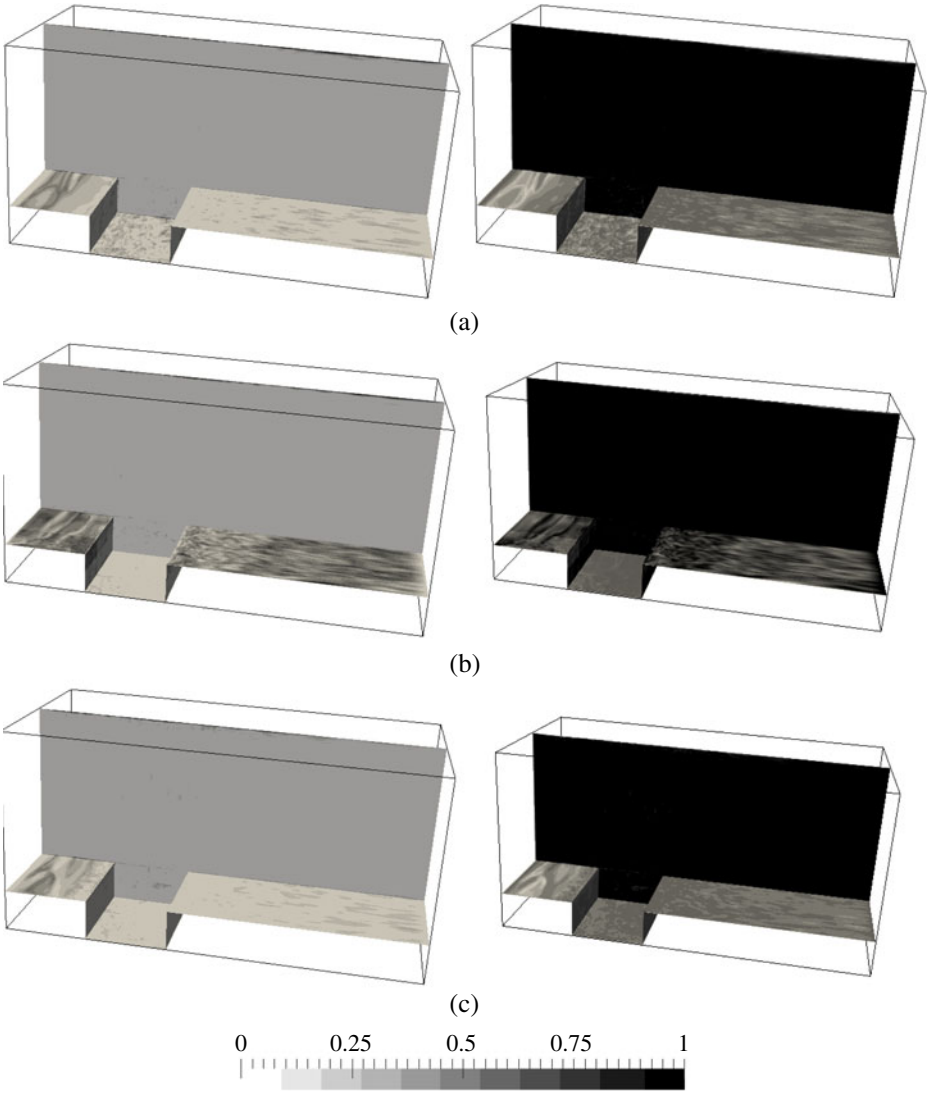

Fig. 34 Maps of the relative contribution of molecular (*left*) and artificial + SGS (*right*) diffusion fluxes to the total energy diffusion fluxes. **a** MiLES. **b** Lagrangian Dynamic Smagorinsky Model with isotropic stress modeling. **c** Vreman model

6 Flow Simulation of a Trapped-Vortex Combustor Geometry

In the flows considered so far, overall the geometries are rather simple; also to increase the test-case complexity, the unsteady flow in a trapped-vortex combustor is now simulated. The geometry of the immersed wall is shown in Fig. 35a, it consists of a main annular flow arriving on a set of rods (flame holder) located before a cavity in which additional fluid is injected through two annular slots, featuring weak flow

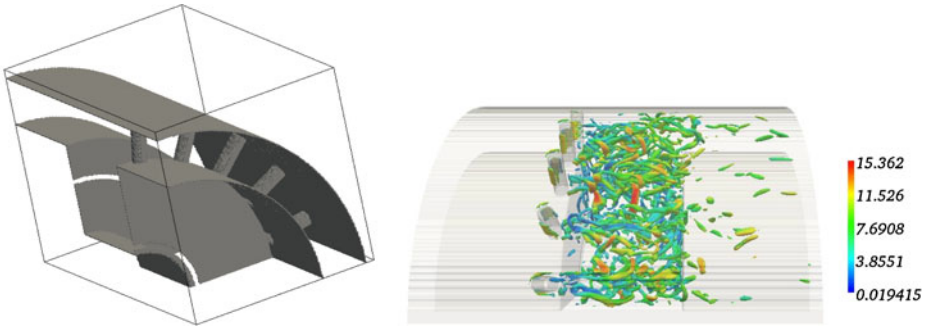

(a) Immersed walls (flow from right to left)

(b) iso-Q (Q=2.19$^7 s^{-2}$) colored by velocity magnitude (flow from left to right)

Fig. 35 **a** Trapped vortex combustor geometry. **b** Flow top-view

rates compared to the main flow. After passing the cavity, the flow leaves the domain as an annular wall confined-jet. Figure 35b presents the complex flow topology with turbulence developing behind the rods, within and above the cavity.

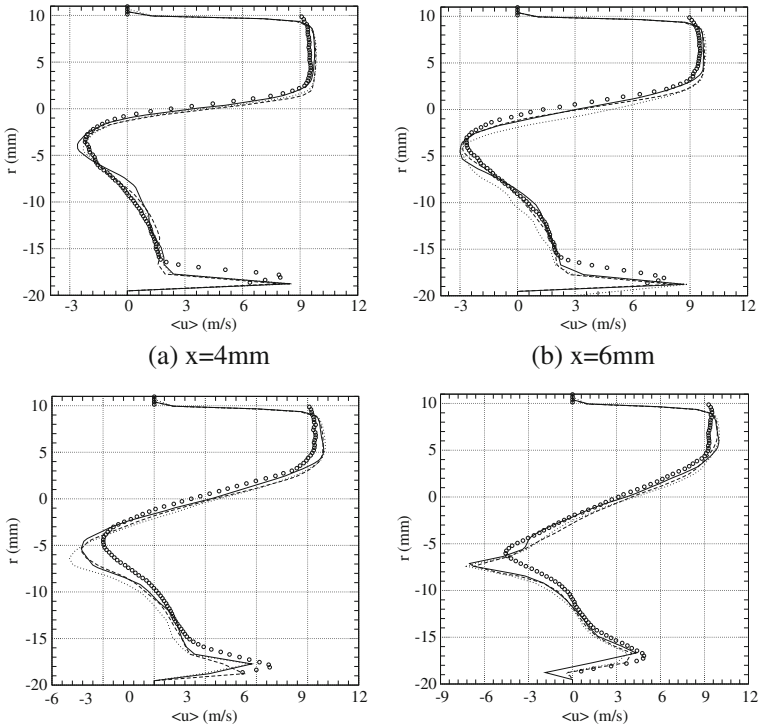

(a) x=4mm (b) x=6mm

(c) x=8mm (d) x=10mm

Fig. 36 Radial profiles of time averaged streamwise velocity between two rods at different streamwise positions. *Dashed line*: MILES. *Dotted line*: VM. *Solid line*: MILES with turbulence injection. *Open circle*: experiments

One quarter of the full geometry is computed, with annular periodicity on the lateral sides of the domain. The length of the cavity is $L = 22$ mm and the computational domain is composed of $3L \times 1.9L \times 1.9L$. The cartesian mesh contains 10,853,864 cells with 43 % devoted to fluid, the LES resolution in the three cartesian directions is 188 μm $< \Delta x <$ 462 μm and $\Delta y = \Delta z =$ 209 μm. A non-reactive case is simulated with an air-flow rate of 20 g/s in the main annular flow, in the cavity 0.7 g/s and 1 g/s are injected through the upstream and downstream annular slots; the main flow velocity is of the order of 10 m/s. Flow measurements inside such a real burner setup are uneasy because of wall complexity, however, magnitude and rms velocity are available in a few planes of the cylindrical system [5].

Time averaged streamwise and rms velocity are given in Figs. 36 and 37 for the Vreman et al. [69] and MILES SGS closures discussed above. Simulations have been performed with and without forcing turbulence [30] at the inlet of the computational domain, however, because many shear layers develop in the vicinity of the rods placed just before the cavity, the inlet forcing procedure was found to have only a weak impact.

The complex flow topology is recovered by the immersed boundary simulations, with a more than fair agreement against measurement considering the complexity of the geometry, for both experimental and numerical investigations.

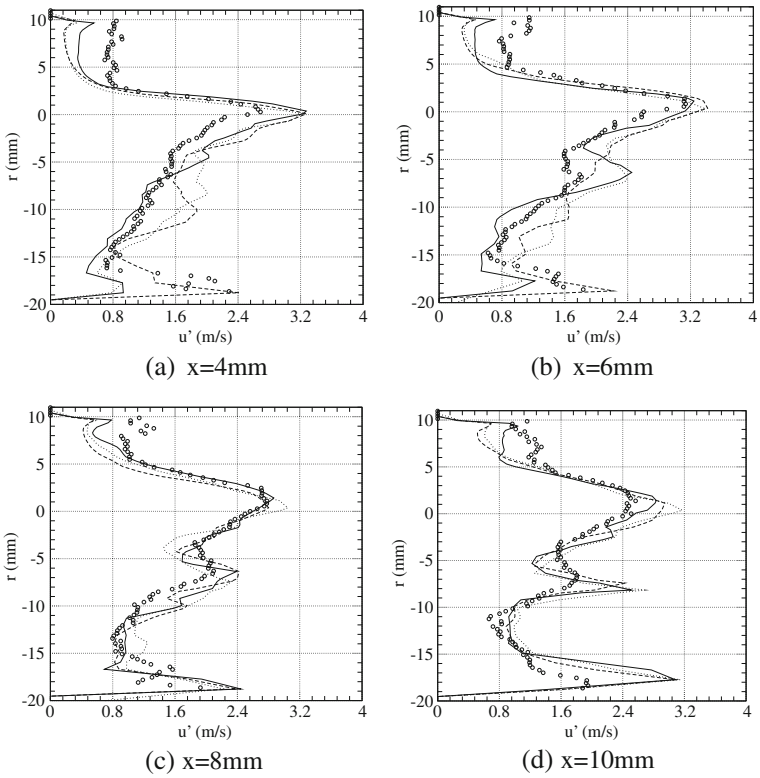

Fig. 37 Radial profiles of velocity RMS between two rods at different streamwise positions. *Dashed line*: MILES. *Dotted line*: VM. *Solid line*: MILES with turbulence injection. *Open circle*: experiments

7 Summary

Considering a set of canonical problems along with a turbulent transonic flow past a cavity, an attempt has been made to demonstrate the potential of an immersed boundaries approach to solve the Navier–Stokes equations in their fully compressible form, with walls arbitrarily imposed over a structured cartesian mesh.

The ghost cell technique plus some adjustments was found to perform well in terms of pressure response and mass conservation, even when the wall is far from conforming to the grid.

After simulating canonical flows (channel inclined over a fixed grid, flow past a cylinder), a transonic cavity flow has been addressed. Large Eddy Simulation was performed with five different approaches for modeling the smallest and unresolved scales. The comparisons with experiments, in particular the power density spectra of pressure fluctuations, demonstrate the full potential of LES with immersed boundaries for a compressible flow. Specifically, the numerical solution reproduces the complex cavity feedback-loop process, which is controlled by the interaction of instabilities in the shear layer with the downstream cavity wall-corner, in relation with the generation of acoustic waves traveling upstream. To address a more complex geometry, a trapped vortex combustor, including rods (flame holder) and a cavity, is also simulated and statistical flow properties compare well with experimental measurements.

Acknowledgements This work was granted access to the HPC resources of IDRIS-CNRS under the allocation 2011-020152 made by GENCI (Grand Equipement National de Calcul Intensif) and was funded by the European research project TECC-AE-FP7 (Technologies Enhancement for Clean Combustion in Aero-Engines), Grant No. 2010-020152. The authors are grateful to Dr. G. Lodato for his precious help in the development of immersed boundary in the flow solver and to Dr. L. Larchevêque for providing detailed information on the transonic cavity flow.

References

1. Balaras, E.: Modeling complex boundaries using an external force field on fixed Cartesian grids in Large Eddy Simulations. Comput. Fluids **33**, 375–404 (2004)
2. Berthelsen, P., Faltinsen, O.: A local directional ghost cell approach for incompressible viscous flow problems with irregular boundaries. J. Comput. Phys. **227**(9), 4354–4397 (2008)
3. Beyer, R.P., Leveque, R.J.: Analysis of a one-dimensional model for the immersed boundary method. SIAM J. Numer. Math. **29**, 332–364 (1992)
4. Burg, J.: Maximum entropy spectral analysis. Ph.D. thesis, Stanford University (1975)
5. Burguburu, J.: Experimental study of flame stability in an aeronautical combustion chamber using trapped burned gases. Ph.D. thesis, National Institute of Applied Sciences Rouen (2012)
6. Capizzano, F.: A turbulent wall model for immersed boundary methods. In: 48th AIAA Aerospace Sciences Meeting Including the New Horizons Forum and Aerospace Exposition. Orlando (2010)
7. Chen, J.H., Pritchard, W.G., Tavener, S.J.: Bifurcation for flow past a cylinder between parallel planes. J. Fluid Mech. **284**, 23 (1995)
8. Choi, J.I., Oberoi, R.C., Edwards, J.R., Rosati, J.A.: An immersed boundary method for complex incompressible flows. J. Comput. Phys. **224**, 757–784 (2007)
9. de Tullio, M.D., Palma, P.D., Iaccarino, G., Pascazio, G., Napolitano, M.: An immersed boundary method for compressible flows using local grid refinement. J. Comput. Phys. **225**(2), 2098–2117 (2007)
10. Domingo, P., Vervisch, L., Deynante, D.: Large Eddy Simulation of a lifted methane jet flame in a vitiated coflow. Combust. Flame **152**, 415–432 (2008)

11. Ducros, F., Ferrand, V., Nicoud, F., Weber, C., Darracq, D., Gacherieu, C., Poinsot, T.: Large Eddy Simulation of the shock/turbulence interaction. J. Comput. Phys. **152**, 517–549 (1999)
12. Ducros, F., Laporte, F., Soulères, T., Guinot, V., Moinat, P., Caruelle, B.: High-order fluxes for conservative skew-symmetric-like schemes in stuctures meshes: application to compressible flows. J. Comput. Phys. **161**, 114–139 (2000)
13. Fadlun, E.A., Verzicco, R., Orlandi, P., Mohd-Yusof, J.: Combined immersed-boundary finite-difference methods for three-dimensional complex flow simulations. J. Comput. Phys. **161**, 35–60 (2000)
14. Forestier, N., Geffroy, P., Jacquin, L.: Etude expérimentale des propriétés instationnaires d'une couche de mélange compressible sur une cavité: cas d'une cavité ouverte peu profonde. Rt 22/00153 *d*afe, ONERA (in French) (2003)
15. Forestier, N., Jacquin, L., Geffroy, P.: The mixing layer over a deep cavity at high-subsonic speed. J. Fluid Mech. **475**, 101–145 (2003)
16. Ghias, R., Mittal, R., Lund, T.S.: A non-body conformal grid method for simulation of compressible flows with complex immersed boundaries. AIAA Paper (2004)
17. Ghias, R., Mittal, R., Dong, H.: A sharp interface immersed boundary method for compressible viscous flows. J. Comput. Phys. **225**, 528–553 (2007)
18. Ghosal, S., Lund, T.S., Moin, P., Akselvoll, K.: A dynamic localization model for large eddy simulation of turbulent flows. J. Fluid Mech. **286**, 229–255 (1995)
19. Gloerfelt, X.: Bruit rayonné par un écoulement affleurant une cavité: simulation aéroacoustique directe et application de méthodes intégrales. Ph.D. thesis, Ecole Centrale de Lyon (2001)
20. Gloerfelt, X.: Cavity noise. In: VKI Lectures: Aerodynamic Noise from Wall-Bounded Flows. Von Karman Institute (2009)
21. Goldstein, D., Handler, R., Sirovich, L.: Modeling a no-slip boundary condition with an external force field. J. Comput. Phys. **105**, 354–366 (1993)
22. Gottlieb, S., Shu, C.: Total variation diminishing runge-kutta schemes. Math. Comput. **67**(221), 73–85 (1998)
23. Grigoriadis, D.G.E., Bratzis, J.G., Goulas, A.: LES of the flow past a rectangular cylinder using the immersed boundary concept. Int. J. Numer. Methods Fluids **41**, 615–632 (2003)
24. Grigoriadis, D.G.E., Bartzis, J.G., Goulas, A.: Efficient treatment of complex geometries for Large Eddy Simulations of turbulent flows. Comput. Fluids **33**, 201–222 (2004)
25. Hu, X., Khoo, B., Adams, N., Huang, F.: A conservative interface method for compressible flows. J. Comput. Phys. **219**(2), 553–578 (2006)
26. Iaccarino, G., Verzicco, R.: Immersed boundary technique for turbulent flow simulations. Appl. Mech. Rev. **56**(3), 331–347 (2003)
27. Jameson, A., Schmidt, W., Turkel, E.: Numerical solutions of the Euler equations by finite volume methods using Runge–Kutta time-stepping schemes. AIAA Paper **1259**, 1981 (1981)
28. Kim, J., Kim, D., Haecheon, C.: An immersed-boundary finite-volume method for simulations of flow in complex geometries. J. Comput. Phys. **171**, 132–150 (2001)
29. Kirkpatrick, M.P., Armfield, S.W., Kent, J.H.: A representation of curved boundaries for the solution of the Navier–Stokes equations on a staggered three-dimensional cartesian grid. J. Comput. Phys. **184**(1), 1–36 (2003)
30. Klein, M., Sadiki, A., Janicka, J.: A digital filter based generation of inflow data for spatially developing direct numerical or Large Eddy Simulation. J. Comput. Phys. **186**, 652–665 (2003)
31. Lai, M.C., Peskin, C.S.: An immersed boundary method with formal second order accuracy and reduced numerical viscosity. J. Comput. Phys. **160**, 705–719 (2000)
32. Laizet, S., Lardeau, S., Lamballais, E.: Direct numerical simulation of a mixing layer downstream a thick plate. Phys. Fluids **22**(1), 015,104 (2003)
33. Lamarque, N., Porta, M., Nicoud, F., Poinsot, T.: On the stability and dissipation of wall boundary conditions for compressible flows. Int. J. Numer. Methods Fluids **62**(10), 1134–1154 (2010)
34. Lamballais, E., Silvestrini, J.: Direct numerical simulation of interactions between a mixing layer and a wake around a cylinder. J. Turbulence **3**, Article Number 028 (2002). doi:10.1088/1468-5248/3/1/028
35. Larchevêque, L., Sagaut, P., Mary, I., Labbé, O.: Large-Eddy Simulation of a compressible flow past a deep cavity. Phys. Fluids. **15**(1), 193–210 (2003)
36. Larchevêque, L., Sagaut, P., Lê, T.H., Comte, P.: Large eddy simulation of a compresible flow in a three dimensional open cavity at high Reynolds number. J. Fluid Mech. **516**, 265–301 (2004)
37. Larchevêque, L., Sagaut, P., Labbé, O.: Large-Eddy Simulation of a subsonic cavity flow including asymmetric three-dimensional effects. J. Fluid Mech. **577**, 105–126 (2007)

38. Lodato, G., Domingo, P., Vervisch, L.: Three-dimensional boundary conditions for direct and Large-Eddy Simulation of compressible viscous flows. J. Comput. Phys. **227**(10), 5105–5143 (2008)
39. Lodato, G., Vervisch, L., Domingo, P.: A compresssible wall-adapting similarity mixed model for Large-Eddy Simulation of the impinging round jet. Phys. Fluids **21**, 035,102 (2009)
40. Lyn, D.A., Einavv, S., Rodi, W., Park, J.H.: A laser-doppler velocimetry study of ensemble-averaged characteristics of the turbulent near wake of a square cylinder. J. Fluid Mech. **304**, 285–319 (1995)
41. Majumdar, S., Iaccarino, G., Durbin, P.: RANS solver with adaptive structured boundary non-conforming grids. In: Annual Research Briefs, pp. 353–366 (2001)
42. Marple, S.L.: Digital Spectral Analysis with Applications. Prentice Hall (1987)
43. McLean, I., Gartshore, I.: Spanwise correlation of pressure on a rigid square section cylinder. J. Wind Eng. **41**, 779–808 (1992)
44. Meneveau, C., Lund, T., Cabot, W.: A Lagrangian dynamic subgrid-scale model of turbulence. J. Fluid Mech. **319**, 353–385 (1996)
45. Meyer, M., Devesa, A., Hickel, S., Adams, N.A.: A conservative immersed interface method for Large-Eddy Simulation of incompressible flows. J. Comput. Phys. **229**, 6300–6317 (2010)
46. Mittal, R., Balanchadar, S.: Effect of intrinsic three-dimensionality on the lift and drag of nominaly two-dimensional cylinders. Phys. Fluids. **7**(8), 1841 (1995)
47. Mittal, R., Dong, H., Bozkurttas, M., Najjar, F., Vargas, A., Von Loebbecke, A.: A versatile sharp interface immersed boundary method for incompressible flows with complex boundaries. J. Comput. Phys. **227**(10), 4825–4852 (2008)
48. Mohd-Yusof, J.: Combined immersed-boundary/B-spline methods for simulations of flow in complex geometries. In: Annual Research Briefs, pp. 317–327 (1997)
49. Moin, P., Squires, K., Cabot, W., Lee, C.: A dynamic subgrid-scale model for compressible turbulence and scalar transport. Phys. Fluids. A **3**(11), 2746–2757 (1991)
50. Murakami, S., Izuka S. ans Ooka, R.: Cfd analysis of turbulent flow past square cylinder using dynamic LES. J. Fluids Struct. **13**, 1097–1112 (1999)
51. Nicoud, F.: Defining wave amplitude in characteristic boundary conditions. J. Comput. Phys. **149**, 418–422 (1999)
52. Palma, P.D., de Tullio, M.D., Pascazio, G., Napolitano, M.: An immersed boundary method for compressible viscous flows. Comput. Fluids **35**(7), 693–702 (2006)
53. Peskin, C.S.: The fluid dynamics of heart valves: experimental, theoretical and computational methods. Annu. Rev. Fluid. Mech. **14**, 135–259 (1982)
54. Poinsot, T., Lele, S.: Boundary conditions for direct simulations of compressible viscous flows. J. Comput. Phys. **101**, 104–129 (1992)
55. Sagaut, P.: Large Eddy Simulation for Incompressible Flows. Springer (2000)
56. Sagaut, P., Garnier, E., Tromeur, E., Larchevêque, L., Labourasse, E.: Turbulent inflow conditions for Large-Eddy Simulation of supersonic and subsonic wall flows. AIAA J. **42**, 469–477 (2004)
57. Sagaut, P., Deck, S., Larchevêque, L.: Numerical simulation data: from validation to physical analysis. In: Congrès Francophone de Technique Laser. CFTL 2008, Futuroscope (2008)
58. Samtaney, R., Pullin, D.I., Kosovic, B.: Direct numerical simulation of decaying compressible turbulence and shocklet statistics. Phys. Fluids **13**, 1415–1430 (2001)
59. Schlichting, H., Gersten, K.: Boundary Layer Theory. Springer, Berlin (2003)
60. Smagorinsky, J.: General circulation experiments with the primitive equations. Mon. Weather Rev. **91**(3), 99–164 (1963)
61. Subramanian, V., Domingo, P., Vervisch, L.: Large-Eddy Simulation of forced ignition of an annular bluff-body burner. Combust. Flame **157**(3), 579–601 (2010)
62. Swanson, R., Turkel, E.: On central-difference and upwind schemes. J. Comput. Phys. **101**(2), 292–306 (1992)
63. Tatsumi, S., Martinelli, L., Jameson, A.: Flux-limited schemes for the compressible Navier–Stokes equations. AIAA J. **33**(2), 252–261 (1995)
64. Thornber, B., Drikakis, D.: Implicit Large-Eddy Simulation of a deep cavity using high-resolution methods. AIAA J. **46**(10), 2634–2645 (2008)
65. Tseng, Y.H., Ferziger, J.H.: LES of 3D turbulent wavy bounadry flow: validation of a ghost-cell immersed boundary method. In: Proc. 3rd International Symposium on Turbulence and Shear Flow Phenomena. Sendai, Japan (2003)

66. Tyagi, M., Acharya, S.: Large Eddy Simulation of turbulent flows in complex and moving rigid geometries using the immersed boundary method. Int. J. Numer. Methods Fluids **48**, 691–722 (2005)
67. Verzicco, R., Mohd-Yusof, J., Orlandi, P., Haworth, D.: LES in complex geometries using boundary body forces. AIAA **38**, 427–433 (2000)
68. Voke, P.R.: Flow past a square cylinder test case LES2, vol. Direct and Large Eddy Simulation II. ERCOFTAC Series (1997)
69. Vreman, A.W.: An eddy-viscosity subgrid-scale model for turbulent shear flow: Algebraic theory and applications, Phys. Fluids **16**(10), 3670–3681 (2004)
70. Ye, T., Mittal, R., Udaykumar, H.S., Shyy, W.: An accurate Cartesian grid method for viscous incompressible flows with complex immersed boundaries. J. Comput. Phys. **156**, 209–240 (1999)
71. Yoshizawa, A.: Statistical theory for compressible turbulent shear flows, with the application to subgrid modeling. Phys. Fluids **29**, 2152–2164 (1986)
72. Zang, Y., Street, R.L., Koseff, J.R.: A dynamic mixed subgrid-scale model and its application to turbulent recirculating flows. Phys. Fluids A **5**(12), 3186–3196 (1993)